Warsaw University of Technology

FACULTY OF ELECTRONICS AND INFORMATION TECHNOLOGY

PhD Thesis

in the discipline of Information and Communication Technology

Few-Shot Human Neural Rendering with Partial Information

Kacper Kania, M.Sc.

supervisor
Tomasz Trzciński, Prof. PhD DSc.

assistant supervisor
Marek Kowalski, PhD DSc.

WARSZAWA 2025

Acknowledgements

Lorem ipsum dolor sit amet, consectetuer adipiscing elit. Ut purus elit, vestibulum ut, placerat ac, adipiscing vitae, felis. Curabitur dictum gravida mauris. Nam arcu libero, nonummy eget, consectetuer id, vulputate a, magna. Donec vehicula augue eu neque. Pellentesque habitant morbi tristique senectus et netus et malesuada fames ac turpis egestas. Mauris ut leo. Cras viverra metus rhoncus sem. Nulla et lectus vestibulum urna fringilla ultrices. Phasellus eu tellus sit amet tortor gravida placerat. Integer sapien est, iaculis in, pretium quis, viverra ac, nunc. Praesent eget sem vel leo ultrices bibendum. Aenean faucibus. Morbi dolor nulla, malesuada eu, pulvinar at, mollis ac, nulla. Curabitur auctor semper nulla. Donec varius orci eget risus. Duis nibh mi, congue eu, accumsan eleifend, sagittis quis, diam. Duis eget orci sit amet orci dignissim rutrum.

Nam dui ligula, fringilla a, euismod sodales, sollicitudin vel, wisi. Morbi auctor lorem non justo. Nam lacus libero, pretium at, lobortis vitae, ultricies et, tellus. Donec aliquet, tortor sed accumsan bibendum, erat ligula aliquet magna, vitae ornare odio metus a mi. Morbi ac orci et nisl hendrerit mollis. Suspendisse ut massa. Cras nec ante. Pellentesque a nulla. Cum sociis natoque penatibus et magnis dis parturient montes, nascetur ridiculus mus. Aliquam tincidunt urna. Nulla ullamcorper vestibulum turpis. Pellentesque cursus luctus mauris.

Nulla malesuada porttitor diam. Donec felis erat, congue non, volutpat at, tincidunt tristique, libero. Vivamus viverra fermentum felis. Donec nonummy pellentesque ante. Phasellus adipiscing semper elit. Proin fermentum massa ac quam. Sed diam turpis, molestie vitae, placerat a, molestie nec, leo. Maecenas lacinia. Nam ipsum ligula, eleifend at, accumsan nec, suscipit a, ipsum. Morbi blandit ligula feugiat magna. Nunc eleifend consequat lorem. Sed lacinia nulla vitae enim. Pellentesque tincidunt purus vel magna. Integer non enim. Praesent euismod nunc eu purus. Donec bibendum quam in tellus. Nullam cursus pulvinar lectus. Donec et mi. Nam vulputate metus eu enim. Vestibulum pellentesque felis eu massa.

Quisque ullamcorper placerat ipsum. Cras nibh. Morbi vel justo vitae lacus tincidunt ultrices. Lorem ipsum dolor sit amet, consectetuer adipiscing elit. In hac habitasse platea dictumst. Integer tempus convallis augue. Etiam facilisis. Nunc elementum fermentum wisi. Aenean placerat. Ut imperdiet, enim sed gravida sollicitudin, felis odio placerat quam, ac pulvinar elit purus eget enim. Nunc vitae tortor. Proin tempus nibh sit amet nisl. Vivamus quis tortor vitae risus porta vehicula.

Abstract

This thesis is a series of publications that introduce novel methods for human neural rendering using limited information, focusing on Neural Radiance Fields (NeRFs) and 3D Gaussian Splatting (3DGS). It explores how these models construct 3D representations from 2D images and demonstrates ways to condition these representations for generating high-quality human renderings. We propose techniques that use simple, interpretable inputs derived from sparse training data and extends these methods to perform effectively in few-shot learning scenarios.

We begin by examining the field of neural radiance fields, addressing limitations in existing approaches and presenting contributions to controllable radiance fields. By incorporating partial and sparse data during training, it leverages the smoothness of neural networks to produce controllable, high-quality human images.

To tackle the reliance on extensive, high-quality data annotations from multi-view videos, we introduce a new method for training neural radiance fields in few-shot, multi-view settings. This approach learns internal deformation templates, which blend smoothly during inference, significantly improving image quality compared to existing baselines and enabling effective human rendering from limited input images.

The work also addresses the need for adaptable computational efficiency during inference. It proposes a fine-to-coarse learning strategy for 3D Gaussian Splatting, which upscales a latent 2D grid that stores Gaussian representations. This strategy achieves competitive results while allowing deployment on various computational devices with minimal quality loss.

In addition, we develop a novel model for controlling radiance fields through environmental lighting. By incorporating precomputed radiance transfer, this model enables physically plausible scene relighting and provides users with intuitive control over lighting in reconstructed scenes.

This research advances the state of the art in controllable neural radiance fields and expands their application to few-shot learning scenarios. These innovations enhance the possibilities for human rendering from limited information and open new directions for future research in the field.

Keywords: Neural Rendering, Neural Radiance Fields, Few-Shot Learning, Human Rendering, Partial Information, Gaussian Splatting

Streszczenie

To jest streszczenie. To jest trochę za krótkie, jako że powinno zająć całą stronę.

Słowa kluczowe: A, B, C

Lay Summary

ok

Publications in this thesis

Title	Authors	Venue	Status
CoNeRF: Controllable Neural Radiance Fields	**Kacper Kania**, Kwang Moo Yi, Marek Kowalski, Tomasz Trzciński, Andrea Tagliasacchi	CVPR 2022	Accepted
BlendFields: Few-Shot Example-Driven Facial Modeling	**Kacper Kania**, Stephan J. Garbin, Andrea Taglisacchi, Virginia Estellers, Kwang Moo Yi, Julien Valentin, Tomasz Trzciński, Marek Kowalski	CVPR 2023	Accepted
LumiGauss: High-Fidelity Outdoor Relighting with 2D Gaussian Splatting	Joanna Kaleta, **Kacper Kania**, Tomasz Trzciński, Marek Kowalski	WACV 2025	Accepted
CLoG: Leveraging UV Space for Continuous Levels of Detail	**Kacper Kania**, Rawal Khirodkar, Shunsuke Saito, Kwang Moo Yi, Julieta Martinez	CVPR 2025	Under Review

Contents

Acknowledgements . . . . . **iii**

Abstract . . . . . **v**

Streszczenie . . . . . **vii**

Lay Summary . . . . . **ix**

Publications in this thesis . . . . . **xi**

Contents . . . . . **xiii**

List of Abbreviations and Symbols **1**

List of Figures **1**

List of Tables **4**

1 Introduction **5**
- 1.1 Motivation and challenges 5
- 1.2 Research objectives 7
- 1.3 Contributions 9
  - 1.3.1 Texture from Partial Information 9
  - 1.3.2 Expression from Few-Shot Learning 10
  - 1.3.3 Light from Unconstrained Images 11
  - 1.3.4 Levels of Detail in One Model 11
- 1.4 Thesis outline 12
- 1.5 Publications not included in the thesis 12

2 Background **13**
- 2.1 Neural Rendering 13
- 2.2 Neural Radiance Field 13
- 2.3 3D Gaussian Splatting 13

3 CoNeRF: Controllable Neural Radiance Fields **15**
- 3.1 Abstract 15

3.2 Introduction . . . 15
3.3 Related works . . . 17
3.3.1 Neural Radiance Field (NeRF) . . . 18
3.3.2 HyperNeRF . . . 18
3.4 Controllable NeRF (CoNeRF) . . . 19
3.4.1 Reconstruction losses . . . 20
3.4.2 Control losses . . . 20
3.4.3 Controlling and rendering images . . . 21
3.4.4 Implementation details . . . 22
3.5 Results . . . 23
3.5.1 Datasets and baselines . . . 23
3.5.2 Comparison with the baselines . . . 25
3.5.3 Direct 2D rendering . . . 27
3.5.4 Ablation study . . . 27
3.6 Conclusions . . . 30
3.7 Acknowledgements . . . 31
3.8 Potential social impact . . . 31
3.9 Architecture details . . . 32
3.10 Failure Cases . . . 32

4 Final remarks and discussion . . . 37
4.1 Conclusions . . . 37
4.2 Future work . . . 37

Bibliography . . . 37

List of Abbreviations and Symbols

List of Figures

1 **Example with annotations and controlled attributes** – We show an example of how our CoNeRF is capable of controlling attributes selected sparse annotations at the training time. Top row shows possible value combinations (− denoting closed eye, 0 neutral position and + an open eye) and $\{\boldsymbol{\beta}_1, \boldsymbol{\beta}_2\}$ possible values of attributes that are not explicitly learned from the annotations but purely from data (please see Chapter 3 for further explanation). 10

2 **Teaser** – We train a controllable neural radiance field from multiple views of a dynamic 3D scene, under varying poses and attributes; in this example eye being open/closed and mouth smiling/frowning. Given only six annotations (a), our method provides full control over the scene appearance, allowing us to synthesize (b) novel views and (c) novel attributes, including attribute combinations that were *never seen* in the training data (green box). 16

3 **Framework** – We depict in (a) the HyperNeRF [58] formulation, and (b) our Controllable-NeRF (CoNeRF). In (a), both point coordinates $\mathbf{x}$ and latent representation $\boldsymbol{\beta}$ are respectively processed by a canonicalizer $\mathcal{K}$ and a hyper map $\mathcal{H}$, which are then turned into radiance and density field values by $\mathcal{R}$. In (b), we introduce regressors $\mathcal{A}$ and $\mathcal{M}$ that regress the attribute and the corresponding mask that enable few-shot attribute-based control of the NeRF model. See Sec. 3.4.3 for details. 19

4 **Novel view and novel attribute synthesis on real data** – We synthesize scenes from a novel view and with a novel attribute combination, not seen during training. A naive extension of HyperNeRF, HyperNeRF+π fails to disentangle attributes and results in a modification of the scene irrespectively of attribute meaning *e.g.*, opening mouth results in closing eyes at the same time. Ours-$\mathcal{M}$ improves the results, but does not disentangles the attribute space, as successfully done by our complete method. The differences between these methods can even lead to complete failure cases, as shown in the metronome and the toy car case. 23

5 **Annotation example** – We provide only a rough annotation for each attribute, which is enough for the method to discover the mask for each attribute across all views automatically. Bottom row shows masks overlaid on the image. 25

6 **Novel view and novel attribute synthesis on synthetic data** – We show examples of novel view and novel attribute synthesis on synthetic data. The scene is composed of three objects, where the color of each object is their attribute. Our method provides control over the color of each object independently, whereas both HyperNeRF+π and Ours-$\mathcal{M}$ fail to deliver controllability and results in all three objects having the same attribute in the rendered scene. 26

7 **2D image generation example** – Our framework also generalizes to direct generation of 2D images. Here we show novel attribute synthesis for a webcam video of a person making expressions. Each individual part of the scene is correctly controlled according to the attribute values. 28

8 **Effect of annotation quality** – Our method is moderately robust to the quality of annotations. We visualize the results for two expressions: frowning and smiling, while keeping both eyes in a neutral position. Even with wildly varying annotations as shown, the reconstructions are reasonably controlled, with the exception of the top row, where we show a case where the annotations is too restrictive, resulting in the annotation being ignored for one eye. We show in bottom row also an interesting case, where the mask is large enough to start capturing the correlation among mouth expressions and the eye. 29

9 **Example with unannotated attributes** – We show an example of how our method performs when a part of the image changes appearance, but is not annotated. With the annotations in (a), we synthesize the scene with novel view and attributes in (b), where the two rows are with different $\boldsymbol{\beta}$ configurations. We denote the attribute configuration on the top of each column in (b). As shown, the change that is not annotated is simply encoded in the per-image encoding $\boldsymbol{\beta}$. 30

10 **Failure cases** – Our model may learn spurious interpolations for controlled elements that occupy little space in the image and with insufficient/careless annotations. For the metronome, due to the fast motion of the pendulum and its specularity, without careful annotation our method may simply learn its motion blur or sometimes even completely ignore the pendulum. In the face example, this may result in the eye blinking multiple times while interpolating between the attribute values of -1 and 1. Both cases are preventable with more careful annotations and by annotating more frames. 32

11 The canonicalization network takes positionally encoded raw coordinates $\mathbf{x}$ and learnable per-image latent code $\boldsymbol{\beta}$ and outputs rotation $\mathbf{r}$ expressed as a quaternion and translation $\mathbf{t}$. We rigidly transform each point $\mathbf{x}$ with an affine transform using both output. We use windowed positional encoding [56] for $\mathbf{x}$ with 8 components, linearly increasing contribution of components throughout 80k steps. We initialize the last layer to small values so the network can learn a base structure of the data. 33

12 The attribute map $\mathcal{A}$ takes a per-image learnable latent code $\boldsymbol{\beta}$ and outputs A attributes $\boldsymbol{\alpha}$. 33

13 The network predicting lifted latent code $\boldsymbol{\beta}$, takes per-image $\boldsymbol{\beta}$ as an input, positionally encoded raw points $\boldsymbol{\beta}$ and outputs a lifted code of size d. We use only one sine component to encode $\mathbf{x}$. 34

14 Per-attributes hypermaps take an attribute together with encoded $\mathbf{x}$ coordinates and output lifted $\alpha_a(\mathbf{x})$ ambient code of size d. We encode $\mathbf{x}$ with only single component. 34

15 Masking network $\mathcal{M}$ take lifted attributes $\boldsymbol{\alpha}(\mathbf{x})$, lifted latent code $\boldsymbol{\beta}(\mathbf{x})$ and canonicalized points $\mathcal{K}(\mathbf{x})$. We transform $\boldsymbol{\alpha}(\mathbf{x})$ and $\boldsymbol{\beta}(\mathbf{x})$ through a windowed positional encoding where we start at 1k-th step linearly increasing a single sine component for the next 10k steps. Points $\mathcal{K}(\mathbf{x})$ are encoded with 8 components. The output is activated with a sigmoid function. We realize $\mathbf{m}_0(\mathbf{x})$ as $\mathbf{m}(\mathbf{x})_0 = 1 - \sum_{a \in A} \mathbf{m}_a(\mathbf{x})$, and clip the output to ensure the values range to be in $[0, 1]$. Note that while the network shares similarities with the radiance field prediction part $\mathcal{R}$, it is not conditioned on view directions and appearance codes. 34

16 The radiance field prediction network predicts RGB colors $\mathbf{c}(\mathbf{x})$ and density values $\sigma(\mathbf{x})$ from canonicalized points. We encode points $\mathbf{x}$ with 8 sine components and linearly increase contribution of a single component in $\boldsymbol{\alpha}(\mathbf{x})$ and $\boldsymbol{\beta}(\mathbf{x})$ from 1k to 11k step. Per-point predicted predicted attributes $\boldsymbol{\alpha}(\mathbf{x})$ and lifted latent code $\boldsymbol{\beta}(\mathbf{x})$ are masked by a mask predicted from the masking network depicted in Fig. 15. The final linear layer takes additional per-image learnable appearance code ψ to account for any visual variations that cannot be explained by the rest of the framework (*e.g.* changes in lighting). The code can discarded during evaluation. The same layer is additionally conditioned on the positionally encoded view directions. We activate the color output with a sigmoid function. 35

List of Tables

1 **Novel view and novel attributes results** – We report average PSNR, MS-SSIM, and LPIPS values for novel view and novel attribute synthesis on synthetic data. Our method gives the best results. 26

2 **Quantitative results (interpolation)** – We report results in terms of PSNR, MS-SSIM, and LPIPS for the interpolation task. These results are obtained for interpolated view synthesis only, not for novel attribute rendering. Our method provides similar performance in terms of rendering quality, but with controllability. 27

3 **Effect of loss functions** – We report the rendering quality of our method as we procedurally introduce the loss terms. For controlled rendering with novel views and attributes (synthetic data), each loss term adds to the rendering quality, with the $\mathcal{L}_{\text{mask}}$ being critical. For the novel view rendering on real data, addition of loss functions for controllability do not have a significant effect on the rendering quality—they do no harm. 28

π	Stała matematyczna równa stosunkowi obwodu okręgu do jego średnicy
I	Natężenie prądu elektrycznego

Chapter 1

Introduction

With the advent of deep learning, research have been exploring varying ways to apply it to computer graphics. One of the most recent and promising approaches is neural rendering. Neural rendering is a field that combines deep learning and computer graphics to generate realistic images of 3D scenes. The neural radiance field (NeRF) is a popular neural rendering technique that represents a 3D scene as a continuous function that maps 3D coordinates to radiance values. NeRF has shown impressive results in generating photorealistic images of 3D scenes. However, NeRF has limitations in terms of memory and computational requirements, which makes it difficult to scale to large scenes.

To alleviate the problem, Kerbl *et al.* [36] proposed a new technique—3D Gaussian Splatting (3DGS). 3DGS is a neural rendering technique that represents a 3D scene as a set of 3D Gaussian that are splatted to an image space using algorithm proposed by Zwicker *et al.* [95]. In contrast to NeRF, 3DGS is more memory efficient and can be used to render large scenes. It can also render scenes with millions of points in real-time on a single GPU.

In this thesis, we focus on those two milestone techniques in neural rendering and address their fundamental problem—lack of controllability.

1.1 Motivation and challenges

NeRF and 3DGS are both impressive techniques that can generate realistic images. However, a single scene representation needs to be trained on a high-end GPU for hours or even days just to render a novel view at the inference time. However, any type of controllability is difficult to achieve with those models. That includes changing the lighting conditions, subject's attributes or even the scene itself. We see imbuing those models with controllability as a an important step towards making them more useful in practice. Our proposed models are designed to address this issue.

One may ask why the controllability is a feat sought after to be researched. We see the inspiration in how human artists work. Imagine an artist working on 3D game where they

need an asset, like a 3D mesh, to be created. Such a mesh takes much effort since it includes modeling, creating a UV map which can then be textured. After the process is finish, the artist's supervisor may task him to change the model to some extent which requires the artist to redo all the effort again. Such a process is not limited to 3D assets as meshes and could be applied to 3DGS or NeRF. However, 3DGS and NeRFs are volumetric in nature. Our exploited and well-established practices no longer apply to them since volumetric representations do not have the underlying surface representation. For that reason, we see a couple of avenues which we explore in this thesis.

Firstly, Park *et al.* [57] proposed NeRFies, a model that creates a volumetric representation of a person from a self-captured sequence with a phone camera. Since the inception of NeRFs [49], it was among the first works the achieved such a high quality of reconstructions from a casual videos. In its primal form, NeRFies were unable to control the avatar in any other way than by a linear interpolation of latent embeddings that embedded the video's time dimension. The follow-up work, HyperNeRF [58] handles this issue by projecting the learnable embeddings with D onto a lower-dimensional space $\mathbb{R}^d$ where $d \ll D$. After the assumption that the $d=2$ is enough to explain the sequence variability, that projected embedding becomes a 2-dimensional space that can be traversed in an interpretable way. However, that space is not intuitive since the projection is a non-linear operation and one cannot predict how values affect the results. To mitigate that issue, we propose to leverage smoothness of Multilayer Perceptrons (MLPs) [57, 73] to constrain the projection via sparse supervision. We realize our approach as a weakly-supervised MLP that out of many images from the sequence (we assume at least 100 frames in our work) only a few are provided with a coarse annotation. Such annotations denote what values a chosen attribute takes and where its effect spans in the image space. We show that our method, which we dubbed CoNeRF [34] and published at the CVPR 2022 conference, imbues NeRFs with a flexible editability feature without the lose of the rendering quality.

Secondly, approaches such as CoNeRF [34], EditNeRF [44] or FigNeRF [82] focus solely on static elements of the scene, hence their controllability is limited to changing colors or textures in general. HyperNeRF [58] arises as a potential solution due to its ability to model object deformations. However, our initial experiments showed that those changes cannot handle motions that affect a subject globally, *e.g.*, jumping jacks performed by a person. To solve the issue, Fang *et al.* [14] proposes to model the deformation via a multi-scale voxel structure which works well in the synthetic setting, such as the one proposed by Pumarola *et al.* [60].

There exists a plethora of works that approach the problem from the another angle—instead of modeling the motion purely from data, they use a template model in the form of a 3D mesh to canonicalize deformed points [93]. Such methods rely on the accuracy of the *registration*, *i.e.*, fitting the template mesh to subject. Since the registration methods [15, 92] are imperfect estimators, they inherently contain registration errors. Those deviations are exacerbated by learnable radiance field models which assume a perfectly calibrated scene. The authors of those approaches usually mitigate the issue with additional latent space [19, 34, 47] that requires

thousands of video frames to learn an avatar of high-fidelity that reacts correctly to deformations such as wrinkles on the forehead. At the same time, performing the registration on the large scale is costly [8]. In this thesis, we seek a remedy for those obstacles. We propose a method that is data-efficient, easy to improve with a minimal user input and can model realistic deformation dependent changes in the subject. Inspired by classical methods in character texturing [54] and motion modeling [39], we propose BlendFields [31], an *homage* to traditional blendshapes [39]. We build on VolTeMorph's [17] approach to point canonicalization to provide a data-efficient way to control the character. We further introduce a physically-based mixture of predefined, learned from data wrinkle templates that represent expression-dependent skin deformations. Our proposed was acknowledged by the reviewers and was accepted to the CVPR 2023 conference.

Thirdly, having the texture and coarse mesh-based controllability, we strive for control scene settings directly. The inverse rendering of 3D scenes is an ill-posed problem where many different lighting settings may explain the same light effects [59]. To facilitate solving the problem, many approaches use datasets of single object's images captured under different lighting conditions [10, 64, 84]. These approaches cannot decouple albedo from the lighting effects [10, 84] or need additional neural networks to predict correct shadows [64] which limits methods' practicality. We propose to use recently proposed 2D Gaussian Splatting [27] which exhibit remarkable quality of the surface reconstruction. Together with our precomputed radiance transfer from classical computer graphics approaches [61, 68], our LumiGauss achieves state-of-the-art reconstruction quality with the ability to render novel lighting conditions with high fidelity. Our work received positive reviews for the WACV 2025 conference.

Finally, volumetric representation are computationally intensive to render, compared to the traditional mesh representation. For NeRFs [49], it takes seven days on V100 NVidia GPU to train for single scene, and more than 60 seconds to render a single image—way beyond any practical applications. Although many approaches have been proposed to speed up the rendering process [18, 24, 51, 62, 85], they usually make a trade-off between memory requirements, quality, and rendering speed. 3D Gaussian Splatting [36] (3DGS) rose as an alternative to NeRF, offering both high-quality rendering at interactive frame rates. However, those frame rates could be achieved with the most advanced GPU units available at that time. As we see the potential in 3DGS to be a viable canonical representation for 3D data, akin to 3D meshes, a need for its adaptability to different computational resources exists. Meshes can be adapted easily with levels of detail (LoD) approaches that remove detail from meshes that do not affect the general object's perception if necessary.

1.2 Research objectives

In this thesis, we explore different avenues of radiance field controllability. With this goal in mind, we aim at answering the following research questions:

(**RQ 1**) Can we imbue a Neural Radiance Field (NeRF) with a controllability by providing sparse annotations to the training dataset? How many annotations suffice to learn smooth interpolation capabilities between controlled values?

(**RQ 2**) Are extreme facial expressions known from the literature sufficient to learn expression-dependent details that extrapolate to expressions unseen at the training time?

(**RQ 3**) Is it possible to learn an underlying radiance transfer function of a scene from images taken in "in-the-wild" setting? Can such a transfer function generalize to unknown environment maps?

(**RQ 4**) How to learn a single 3D Gaussian Splatting (3DGS) representation that can be adapted to different computational regimes at inference time in a feed-forward mode?

Each of these questions is a representative of possible among many others controllability directions for radiance fields. In case of this thesis, we present summarize our methods as controls of: texture [31, 34], shape [31], lightning [30] and use of resources [32]. To answer (**RQ 1**), we describe our CoNeRF [34]. It is one of the pioneering works that uses sparsely annotated frames to continuously control the subject in a post-hoc manner. We leverage the fact that MLP used in NeRFs are smooth functions biased towards low frequency signals [73]. For that reason, NeRF can learn to interpolate smoothly the annotation signal between frames of high similarity. We show that this assumption is sufficient to obtain both novel view synthesis and novel attribute synthesis with a single model.

We further move towards answering (**RQ 2**). We introduce BlendFields [31], achieving two primary goals: ability to generalize unknown expressions via a predefined face mesh template, and a mixture model of training expressions that can produce spatially coherent, expression-dependent wrinkles on the face from as few as three expressions. In our work, we build on VolTeMorph [17] to achieve to former, and focus on the latter contribution. Inspired by texture maps in classical computer graphics pipelines [54], we define a set of learnable radiance fields, each being overfit to a particular extreme expression from the training set. We define an extreme expression as one of the possible expressions involving the most facial muscles. Building on VolTeMorph [17] allows us to use an underlying tetrahedral mesh to compute physical quantities such as the volume change of tetrahedra under a given expression. We use those quantities to linearly interpolate between the pretrained radiance fields. We mix the tetrahedra independently which makes rendering novel expressions possible. For example, BlendFields can render one of the eyebrows raised while maintaining the other in a natural position, which is a difficult expression to make for majority of people.

Our LumiGauss [30] answers (**RQ 3**). In contrary to common approaches [64], we posit that the radiance transfer function known among computer graphics researchers [61] can be learned from unconstrained photo collection under varying lighting conditions. To this end, we use 2DGS [27] which gives us a smooth shape representation, difficult to achieve when

using 3DGS [36]. With the use of contributed priors, we induce learning Gaussian's Spherical Harmonics such that they correctly react to changing environment maps. Not only our approach is fast to train, but renders realistic scenes and object's shadows even under novel lighting conditions.

All the contributions so far are affected by a specific disadvantage—a single model needs to be trained from scratch and it can be deployed only on high-end hardware. We then ask if we can train a single model that is adaptable at inference time to different hardware regimes (**RQ 4**). We propose CLoG [32] as a potential remedy. Our approach uses the fact that one can constrain the number of Gaussians in 3DGS [36] to a specific number, such that it can be formed as a 2D grid by simple reshape operation. With a specific training coarse-to-fine training protocol we contributed, the model learns a representation that converges to a high-quality volumetric structure. In the second training stage, we leverage the fact that Gaussians's can be spatially sorted in such a manner that their descriptors are placed next to each other if they are similar. That forms a low-frequency image which can be modulated with an off-the-shelf continuous upsampling architecture [78]. The architecture outputs a new grid of the given resolution. We show in our work that such an approach achieves remarkable results and can output any number of Gaussians at inference time with high quality.

1.3 Contributions

Building on those questions, we structure this thesis in several chapters corresponding to the answers. An answer is in a form of a scientific article where we introduce the following:

- A novel approach for controlling trained radiance fields with the use of sparsely annotated images from a casually captured data.
- A new model capable of blending trained radiance fields from multi-view frames in an interpretable way and extrapolating to novel human expressions for the trained subject.
- The first use of Gaussian Splatting methods that learns a coherent shape representation of a subject and an ability to distill the varying lighting conditions in the data to a radiance transfer function.
- A novel paradigm for learning Gaussian Splatting models as 2D grids to achieve flexibility to adapt the model to different computational regimes at inference time.

1.3.1 Texture from Partial Information

Existing NeRF-based approaches in 2021 were simple models—they were overfit to a single subject, for a new subject the model needed to be retrained from scratch, and the editability

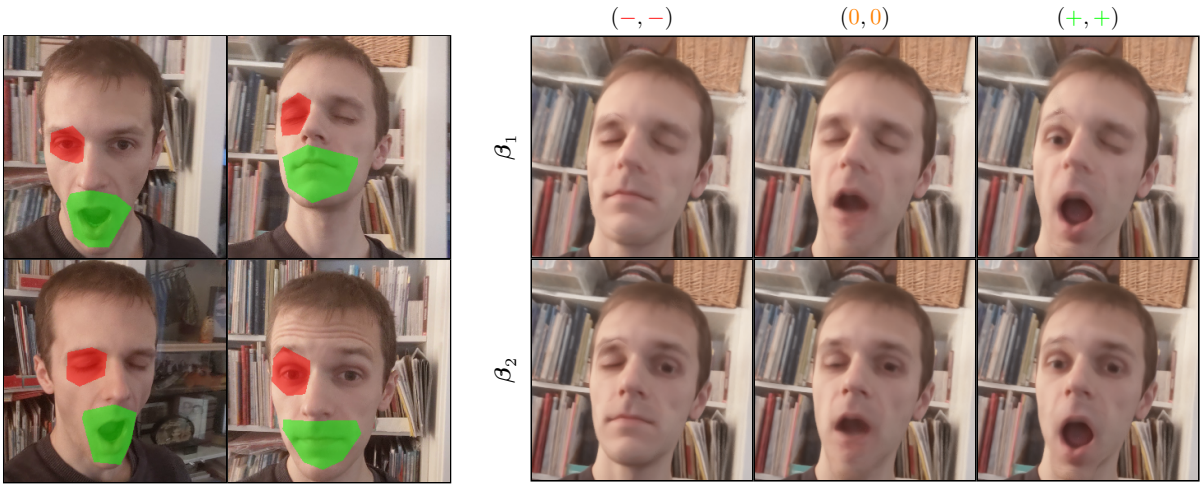

(a) annotated samples **(b)** renderings from the trained model

Figure 1. Example with annotations and controlled attributes – We show an example of how our CoNeRF is capable of controlling attributes selected sparse annotations at the training time. Top row shows possible value combinations ($-$ denoting closed eye, 0 neutral position and $+$ an open eye) and $\{\boldsymbol{\beta}_1, \boldsymbol{\beta}_2\}$ possible values of attributes that are not explicitly learned from the annotations but purely from data (please see Chapter 3 for further explanation).

capabilities were limited [44]. NeRFactor [90] could be considered a more sophisticated model. However, it worked only for simple scene with calibrated scenes and could not handle any motion.

We approach those issues in our CoNeRF [34] published at the CVPR 2021 conference. Inspired by HyperNeRF [58], we propose to revisit the weak supervision in the context of radiance fields. Specifically, under an assumption that one can provide a few of sparse annotations to the dataset, we can leverage the smoothness of the neural networks to propagate the annotation across the dataset. The annotations also consist of what regions in the image space it refers to and hence we can train a semantic segmentation radiance fields that decouples attribute controls. We show an example in Fig. 1 where the left side represents the annotations present in the data and the right one possible manipulations at the inference time. We note that those annotations are easy to make in a matter of a few minutes for a single dataset. However, the complexity of the annotations grows with the number of attributes to control.

1.3.2 Expression from Few-Shot Learning

CoNeRF [34] is capable of rendering complex motions given sufficient amount of data and provided annotations. However, motions as the ones a person performs daily when speaking are infeasible in practice. We propose a solution to target that issue. We introduce BlendFields [31] from the CVPR 2023 proceedings which learns motion-dependent face deformation from data. We build on VolTeMorph [17] which uses existing face template models, such as FLAME [41], to learn a single canonical representation, akin to the canonicalization module in CoNeRF. Internally, BlendFields creates a tetrahedral cage around the face model. For each sample

along the ray in NeRF, it moves the points to a "neutral position", chosen once prior to the training procedure. Such a procedure comes insufficient to model realistic facial features, such as wrinkles. We contribute a novel approach to modeling those deformations. We compute a deformation gradient of each tetrahedra for a given expression which is a physically-based and easy to interpret quantity. The value serves us to smoothly transition face regions textures to appropriate colors. We obtain the colors from NeRFs branches, each overfit to particular expression. In principle, BlendFields predicts face bases which are conditioned on the face expression vector to output the final point color. Our framework works well even when only a few "extreme" expressions are provided such as grinning face with closed eyes and wide open mouth with open eyes.

1.3.3 Light from Unconstrained Images

In both approaches above, we tackle the problem of texture controllability. They assume an ideal case scenario where a capture can be taken in an idealized environment with constant camera exposure and lighting. Moreover, the produced colors are blended together, making the change of light impossible in practice. We then ask the questions if we can decouple an intrinsic color of the subject and change of that color stemming from the environment light. We answer that question with our LumiGauss [30] published at the WACV 2025 conference that, indeed, we can achieve that by learning the radiance transfer function directly from data. For that end, we train a 2DGS [27] model to obtain a smooth and spatially coherent surface of objects. On top of the other attributes known from 3DGS [36], we imbue our Gaussians with additional features corresponding to the radiance transfer, expressed as Spherical Harmonics [20]. We show in our experiments that such a formulation is sufficient to train a model that reacts to changing environment maps in a realistic manner and renders images of higher fidelity than prior approaches.

1.3.4 Levels of Detail in One Model

All the contributions above require considerable computation hardware to be trained on and then run inference in near real-time frame rates. Drawing an inspiration from the gaming industry where Levels of Details (LoD) for meshes is used heavily, we introduce CLoG [32]. Our approach trains a single Gaussian Splatting model such that it can be modulated at inference time and adapted to the target computational requirements with a minimal loss on the rendering quality. That allows us to democratize the use of 3DGS and deploy a single model even on handheld devices. We show later that even under a strict case where only 2,000 Gaussians[1] can be used, the object is still recognizable. The most important contribution of our model is that it is continuous by design while the existing baselines assume prior the training the model how many LoD the model should comprise at inference. To change the size of particular LoD in those

[1] Common 3DGS models can achieve from 10^5 to even 10^6 Gaussians.

baselines requires training the whole model from scratch, imposing a significant computational burden.

1.4 Thesis outline

This thesis is structured as follows. We start by introducing the preliminaries related to the Neural Radiance Fields and Gaussian Splatting in Chapter 2—a common theme in all works that appear later. We then move towards describing CoNeRF [34] in Chapter 3, our approach to control trained neural radiance fields by using sparse annotations. In **??**, we describe BlendFields [31] that can produce realistic expression-dependent texture from just a few multi-view frames of the subjects. **??** introduces the LumiGauss [30], a Gaussian Splatting model that learns a radiance transfer function for novel lighting rendering capabilities. Finally, we bring a general method, CLoG [32], that uses Gaussian Splatting to learn continuous levels of detail while training only a single model. We conclude the thesis in Chapter 4 where we also explore possible future avenues that can be undertaken.

1.5 Publications not included in the thesis

We attach a list of articles that are related to and can be used to in neural rendering approaches:

- **Kania**, **K.**, Zięba, M., and Kajdanowicz, T., "UCSG-NET – Unsupervised Discovering of Constructive Solid Geometry Tree," *NeurIPS*, vol. 33, pp. 8776–8786, 2020,
- **Kania**, **K.**, Kowalski, M., and Trzciński, T., "TrajeVAE: Controllable Human Motion Generation from Trajectories," *arXiv preprint arXiv:2104.00351*, 2021,
- Stypułkowski, M., **Kania**, **K.**, Zamorski, M., Zięba, M., Trzciński, T., and Chorowski, J., "Representing Point Clouds with Generative Conditional Invertible Flow Networks," *Pattern Recognition Letters*, vol. 150, pp. 26–32, 2021,
- Xia, S., Yue, J., **Kania**, **K.**, Fang, L., Tagliasacchi, A., Yi, K. M., and Sun, W., "Densify Your Labels: Unsupervised Clustering with Bipartite Matching for Weakly Supervised Point Cloud Segmentation," *arXiv preprint arXiv:2312.06799*, 2023,
- Esposito, S., Xu, Q., **Kania**, **K.**, Hewitt, C., Mariotti, O., Petikam, L., Valentin, J., Onken, A., and Mac Aodha, O., "GeoGen: Geometry-Aware Generative Modeling via Signed Distance Functions," in *CVPRW*, 2024, pp. 7479–7488,
- Spurek, P., Winczowski, S., Zięba, M., Trzciński, T., **Kania**, **K.**, and Mazur, M., "Modeling 3D Surfaces with a Locally Conditioned Atlas," in *ICCS*, Springer, 2024, pp. 100–115.

Chapter 2

Background

2.1 Neural Rendering

2.2 Neural Radiance Field

2.3 3D Gaussian Splatting

Chapter 3

CoNeRF: Controllable Neural Radiance Fields

3.1 Abstract

We extend neural 3D representations to allow for intuitive and interpretable user control beyond novel view rendering (i.e. camera control). We allow the user to annotate which part of the scene one wishes to control with just a small number of mask annotations in the training images. Our key idea is to treat the attributes as latent variables that are regressed by the neural network given the scene encoding. This leads to a few-shot learning framework, where attributes are discovered automatically by the framework, when annotations are not provided. We apply our method to various scenes with different types of controllable attributes (e.g. expression control on human faces, or state control in movement of inanimate objects). Overall, we demonstrate, to the best of our knowledge, for the first time novel view and novel attribute re-rendering of scenes from a single video.

3.2 Introduction

Neural radiance field (NeRF) [49] methods have recently gained popularity thanks to their ability to render photorealistic novel-view images [47, 56, 58, 87]. In order to widen the scope to other possible applications, such as digital media production, a natural question is whether these methods could be extended to enable *direct* and *intuitive* control by a digital artist, or even a casual user. However, current techniques only allow coarse-grain controls over materials [90], color [28], or object placement [83], or only support changes that they are designed to deal with, such as shape deformations on a learned shape space of chairs [44], or are limited to facial expressions encoded by an explicit face model [16]. By contrast, we are interested in *fine-grained* control without limiting ourselves to a specific class of objects or their properties. For example, given a self-portrait video, we would like to be able to control individual *attributes* (e.g. whether

(a) annotations **(b)** novel views **(c)** novel attributes

Figure 2. Teaser – We train a controllable neural radiance field from multiple views of a dynamic 3D scene, under varying poses and attributes; in this example eye being open/closed and mouth smiling/frowning. Given only six annotations (a), our method provides full control over the scene appearance, allowing us to synthesize (b) novel views and (c) novel attributes, including attribute combinations that were *never seen* in the training data (green box).

the mouth is open or closed); see Fig. 2. We would like to achieve this objective with minimal user intervention, without the need of specialized capture setups [43].

However, it is unclear how fine-grained control can be achieved, as current state-of-the-art models [58] encode the structure of the 3D scene in a *single* and *not interpretable* latent code. For the example of face manipulation, one could attempt to resolve this problem by providing *dense* supervision by matching images to the corresponding Facial Action Coding System (FACS) [12] action units. Unfortunately, this would require either an automatic annotation process or careful and extensive per-frame human annotations, making the process expensive, generally unwieldy, and, most importantly, domain-specific. Automated tools for domain-agnostic latent disentanglement are a very active topic of research in machine learning [9, 25, 26], but no effective plug-and-play solution exists yet.

Conversely, we borrow ideas from 3D morphable models (3DMM) [5], and in particular to recent extensions that achieve local control by *spatial disentanglement* of control attributes [52, 80]. Rather than having a single global code controlling the expression of the *entire* face, we would like to have a set of *local* "attributes", each controlling the corresponding *localized* appearance; more specifically, we assume spatial quasi-conditional independence of attributes [80]. For our example in Fig. 2, we seek an attribute capable to control the appearance of the mouth, another to control the appearance of the eye, etc.

Thus, we introduce a learning framework denoted CoNeRF (i.e. Controllable NeRF) that is capable of achieving this objective with just *few-shot* supervision. As illustrated in Fig. 2, given a single one-minute video, and with as little as two annotations per attribute, CoNeRF allows *fine-grained*, *direct*, and *interpretable* control over attributes. Our core idea is to provide, on top of the ground truth attribute tuple, *sparse* 2D mask annotations that specify which region of the image an attribute controls, in spirit of Interactive Digital Photomontage [1] and Video Sprites [66]. Further, by treating attributes as latent variables within the framework, the mask

annotations can be automatically propagated to the whole input video. Thanks to the quasi-conditional independence of attributes, our technique allows us to synthesize expressions that were *never* seen at training time; e.g. the input video never contained a frame where both eyes were closed and the actor had a smiling expression; see Fig. 2 (green box).

Contributions To summarize, our CoNeRF method[1]:

- provides *direct*, *intuitive*, and *fine-grained* control over 3D neural representations encoded as NeRF;
- achieves this via *few-shot* supervision, *e.g.*, just a handful of annotations in the form of attribute values and corresponding 2D mask are needed for a one minute video;
- while inspired by domain-specific facial animation research [80], it provides a *domain-agnostic* technique.

3.3 Related works

Neural Radiance Fields [49] provide high-quality renderings of scenes from novel views with just a few exemplar images captured by a handheld device. Various extensions have been suggested to date. These include ones that focus on improving the quality of results [47, 56, 58, 87], ones that allow a single model to be used for multiple scenes [67, 77], and some considering controllability of the rendering output at a coarse level [22, 44, 82, 83, 86, 90], as we detail next.

In more detail, existing works enable only compositional control of object location [83, 86], and recent extensions also allow for finer-grain reproduction of global illumination effects [22]. NeRFactor [90] shows one can model albedos and BRDFs, and shadows, which can be used to, *e.g.*, edit material, but the manipulation they support is limited to what is modeled through the rendering equation. CodeNeRF [28] and EditNeRF [44] showed that one can edit NeRF models by modifying the shape and appearance encoding, but they require a curated dataset of objects viewed under different views and colors. HyperNeRF [58], on the other hand can adapt to unseen changes specific to the scene, but learns an arbitrary attribute (ambient) space that cannot be supervised, and, as we show in Sec. 3.5, cannot be easily related to specific local attribute within the scene for controllability.

Explicit supervision One can also condition NeRF representations [16] with face attribute predicted by pre-trained face tracking networks, such as Face2Face [75]. Similarly, for human bodies, A-NeRF [71] and NARF [53] use the SMPL [45] model to generate interpretable pose parameters, and Neural Actor [43] further includes normal and texture maps for more detailed rendering. While these models result in controllable NeRF, they are limited to domain-specific control and the availability of a heavily engineered control model.

[1] Code and dataset are released here.

Controllable neural implicits Controllability of neural 3D *implicit* representations has also been addressed by the research community. Many works have limited focus on learning *human* neural implicit representations while enabling the control via SMPL parameters [45], or linear blend skinning weights [2, 11, 23, 46, 48, 65, 91, 94]. Some initial attempts at learned disentangled of shape and poses have also been made in A-SDF [50], allowing behavior control of the output geometry (*e.g.* doors open vs. closed) while maintaining the general shape. However, the approach is limited to controlling SE(3) articulation of objects, and requires dense 3D supervision.

3.3.1 Neural Radiance Field (NeRF)

For completeness, we briefly discuss NeRF before diving into the details of our method. A Neural Radiance Field captures a volumetric representation of a specific scene within the weights of a neural network. As input, it receives a sample position $\mathbf{x}$ and a view direction $\mathbf{v}$ and outputs the density of the scene σ at position $\mathbf{x}$ as well as the color $\mathbf{c}$ at position $\mathbf{x}$ as seen from view direction $\mathbf{v}$. One then renders image pixels $\mathbf{C}$ via volume rendering [29]. In more detail, $\mathbf{x}$ is defined by observing rays $\mathbf{r}(t)$ as $\mathbf{x} = \mathbf{r}(t)$, where t parameterizes at which point of the ray you are computing for. One then renders the color of each pixel $\mathbf{C}(\mathbf{r})$ by computing

$$\mathbf{C}\left(\mathbf{r}\right) = \int_{t_n}^{t_f} T(t)\sigma\left(\mathbf{r}(t)\right)\mathbf{c}\left(\mathbf{r}(t), \mathbf{v}\right) dt \ , \tag{1}$$

where $\mathbf{v}$ is the viewing angle of the ray $\mathbf{r}$, t_n and t_f are the near and far planes of the rendering volume, and

$$T(t) = \exp\left(-\int_{t_n}^{t} \sigma(\mathbf{r}(s))ds\right) \ , \tag{2}$$

is the accumulated transmittance. Integration in Eq. (1) is typically done via numerical integration [49].

3.3.2 HyperNeRF

Note that in its original formulation Eq. (1) is only able to model *static* scenes. Various recent works [56, 58, 76] have been proposed to explicitly account for possible appearance changes in a scene (for example, temporal changes in a video). To achieve this, they introduce the notion of *canonical hyperspace* – more formally given a 3D query point $\mathbf{x}$ and the collection $\boldsymbol{\theta}$ of all parameters that describe the model, they define:

$$\mathcal{K}(\mathbf{x}) \equiv \mathcal{K}(\mathbf{x}; \boldsymbol{\beta}, \boldsymbol{\theta}), \qquad \text{Canonicalizer} \tag{3}$$

$$\boldsymbol{\beta}(\mathbf{x}) \equiv \mathcal{H}(\mathbf{x}; \boldsymbol{\beta}, \boldsymbol{\theta}), \qquad \text{Hyper Map} \tag{4}$$

$$\mathbf{c}(\mathbf{x}), \sigma(\mathbf{x}) = \mathcal{R}(\mathcal{K}(\mathbf{x}), \boldsymbol{\beta}(\mathbf{x}); \boldsymbol{\theta}). \qquad \text{Hyper NeRF} \tag{5}$$

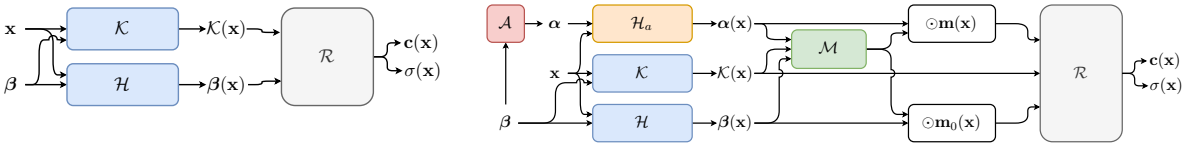

(a) Neural radiance field with lifting [58] **(b)** Controllable neural radiance field (our method)

Figure 3. Framework – We depict in (a) the HyperNeRF [58] formulation, and (b) our Controllable-NeRF (CoNeRF). In (a), both point coordinates $\mathbf{x}$ and latent representation $\boldsymbol{\beta}$ are respectively processed by a canonicalizer $\mathcal{K}$ and a hyper map $\mathcal{H}$, which are then turned into radiance and density field values by $\mathcal{R}$. In (b), we introduce regressors $\mathcal{A}$ and $\mathcal{M}$ that regress the attribute and the corresponding mask that enable few-shot attribute-based control of the NeRF model. See Sec. 3.4.3 for details.

where the location is canonicalized via a canonicalizer $\mathcal{K}$, and the appearances, represented by $\boldsymbol{\beta}$, are mapped to a hyperspace via $\mathcal{H}$, which are then utilized by another neural network $\mathcal{R}$ to retrieve the color $\mathbf{c}$ and the density σ at the query location. Note throughout this paper we denote $\boldsymbol{\beta}$ to indicates a latent code, while $\boldsymbol{\beta}(\mathbf{x})$ to indicate the corresponding field generated by the hypermap lifting. With this latent lifting, these methods render the scene via Eq. (1). Note that the original NeRF model can be thought of the case where $\mathcal{K}$ and $\mathcal{H}$ are identity mappings.

3.4 Controllable NeRF (CoNeRF)

Given a collection of C color images $\{\mathbf{C}_c\} \in [0,1]^{W\times H\times 3}$, we train our controllable neural radiance field model by an auto-decoding optimization [55] whose losses can be grouped into two main subsets:

$$\underset{\boldsymbol{\theta}=\boldsymbol{\theta},\{\boldsymbol{\beta}_c\}}{\arg\min} \underbrace{\mathcal{L}_{\text{rep}}(\boldsymbol{\theta};\{\mathbf{C}_c\})}_{\text{Sec. 3.4.1}} + \underbrace{\mathcal{L}_{\text{ctrl}}(\boldsymbol{\theta};\{\mathbf{M}^{\text{gt}}_{c,a}\},\{\alpha^{\text{gt}}_{c,a}\})}_{\text{Sec. 3.4.2}}. \tag{6}$$

The first group consists of the classical HyperNeRF [58] auto-decoder losses, attempting to optimize neural network parameters $\boldsymbol{\theta}$ jointly with latent codes $\{\boldsymbol{\beta}_c\}$ to *reproduce* the corresponding input images $\{\mathbf{C}_c\}$:

$$\mathcal{L}_{\text{rep}}(\cdot) = \mathcal{L}_{\text{recon}}(\boldsymbol{\theta},\{\boldsymbol{\beta}_c\};\{\mathbf{C}_c\}) + \mathcal{L}_{\text{enc}}(\{\boldsymbol{\beta}_c\}). \tag{7}$$

The latter allow us to inject *explicit control* into the representation, and are our core contribution:

$$\mathcal{L}_{\text{ctrl}}(\cdot) = \mathcal{L}_{\text{mask}}(\boldsymbol{\theta},\{\boldsymbol{\beta}_c\};\{\mathbf{M}^{\text{gt}}_{c,a}\}) \qquad \text{g.t. masks} \tag{8}$$

$$+ \mathcal{L}_{\text{attr}}(\boldsymbol{\theta},\{\boldsymbol{\beta}_c\};\{\alpha^{\text{gt}}_{c,a}\}). \qquad \text{g.t. attributes} \tag{9}$$

As mentioned earlier in Sec. 3.2, we aim for a neural 3D appearance model that is controlled by a collection of attributes $\boldsymbol{\alpha}=\{\alpha_a\}$, and we expect each image to be a manifestation of a different value of attributes, that is, each image $\mathbf{C}_c$, and hence each latent code $\boldsymbol{\beta}_c$, will have a

corresponding attribute $\boldsymbol{\alpha}_c$. The learnable connection between latent codes $\boldsymbol{\beta}$ and the attributes $\boldsymbol{\alpha}$, which we represent via regressors, is detailed in Sec. 3.4.3.

3.4.1 Reconstruction losses

The primary loss guiding the training of the NeRF model is the reconstruction loss, which simply aims to reconstruct observations $\{\mathbf{C}_c\}$. As in other neural radiance field models [47, 49, 56, 58] we simply minimize the L2 photometric reconstruction error with respect to ground truth images:

$$\mathcal{L}_{\text{recon}}(\cdot) = \sum_c \mathbb{E}_{\mathbf{r}\sim\mathbf{C}_c}\left[\left\|\mathbf{C}(\mathbf{r};\boldsymbol{\beta}_c,\boldsymbol{\theta}) - \mathbf{C}^{\text{gt}}(\mathbf{r})\right\|_2^2\right]. \tag{10}$$

As is typical in auto-decoders, and following [55], we impose a zero-mean Gaussian prior on the latent codes $\{\boldsymbol{\beta}_c\}$:

$$\mathcal{L}_{\text{enc}}(\cdot) = \sum_c \|\boldsymbol{\beta}_c\|_2^2. \tag{11}$$

3.4.2 Control losses

The user defines a *discrete* set of A number of attributes that they seek to control, that are *sparsely* supervised across frames—we only supervise attributes *when* we have an annotation, and let others be discovered on their own throughout the training process, as guided by Eq. (7). More specifically, for a particular image $\mathbf{C}_c$, and a particular attribute α_a, the user specifies the quantities:

- $\alpha_{c,a} \in [-1, 1]$: specifying the value for the a-th attribute in the c-th image; see the *sliders* in Fig. 2;
- $\mathbf{M}_{c,a} \in [0,1]^{W\times H}$: roughly specifying the image region that is controlled by the a-th attribute in the c-th image; see the *masks* in Fig. 2.

To formalize sparse supervision, we employ an indicator function $\delta_{c,a}$, where $\delta_{c,a} = 1$ if an annotation for attribute a for image c is provided, otherwise $\delta_{c,a} = 0$. We then write the loss for *attribute* supervision as:

$$\mathcal{L}_{\text{attr}}(\cdot) = \sum_c \sum_a \delta_{c,a} |\alpha_{c,a} - \alpha_{c,a}^{\text{gt}}|^2. \tag{12}$$

For the mask few-shot supervision, we employ the volume rendering in Eq. (20) to project the 3D volumetric neural mask field $\mathbf{m}_a(\mathbf{x})$ into image space, and then supervise it as:

$$\mathcal{L}_{\text{mask}}(\cdot) = \sum_{c,a} \delta_{c,a}\, \mathbb{E}_{\mathbf{r}}\left[\text{CE}\left(\mathbf{M}(\mathbf{r};\boldsymbol{\beta}_c,\boldsymbol{\theta}), \mathbf{M}_{c,a}^{\text{gt}}(\mathbf{r})\right)\right], \tag{13}$$

where $\text{CE}(\cdot,\cdot)$ denotes cross entropy, and the field $\sigma(\mathbf{x})$ in Eq. (20) is learned by minimizing Eq. (10). Importantly, as we do not wish for Eq. (13) to interfere with the training of the underlying 3D representation learned through Eq. (10), we *stop gradients* in Eq. (13) w.r.t.

$\sigma(\mathbf{x})$. Furthermore, in practice, because the attribute mask vs. background distribution can be highly imbalanced depending on which attribute the user is trying to control (*e.g.* an eye only covers a very small portion of an image), we employ a *focal loss* [42] in place of the standard cross entropy loss.

3.4.3 Controlling and rendering images

In what follows, we drop the image subscript c to simplify notation without any loss of generality. Given a B-dimensional latent code $\boldsymbol{\beta}$ representing the 3D scene behind an image, we derive a mapping to our A attributes via a neural map $\mathcal{A}$ with learnable parameters $\boldsymbol{\theta}$:

$$\{\alpha_a\} = \mathcal{A}(\boldsymbol{\beta}; \boldsymbol{\theta}), \quad \mathcal{A} : \mathbb{R}^B \rightarrow [0,1]^A, \tag{14}$$

where these correspond to the *sliders* in Fig. 2. In the same spirit of Eq. (4), to allow for complex topological changes that may not be represented by the change in a single scalar value alone, we lift the attributes to a hyperspace. In addition, since each attribute governs different aspects of the scene, we employ *per-attribute* learnable hypermaps $\{\mathcal{H}_a\}$, which we write:

$$\alpha_a(\mathbf{x}) = \mathcal{H}_a(\mathbf{x}, \alpha_a; \boldsymbol{\theta}) \quad \mathcal{H}_a : \mathbb{R}^3 \times \mathbb{R} \rightarrow \mathbb{R}^d. \tag{15}$$

Note that while α_a is a scalar *value*, $\alpha_a(\mathbf{x})$ is a *field* that can be queried at any point $\mathbf{x}$ in space. These fields are concatenated to form $\boldsymbol{\alpha}(\mathbf{x}) = \{\alpha_a(\mathbf{x})\}$.

We then provide all this information to generate an *attribute masking field* via a network $\mathcal{M}(\cdot; \boldsymbol{\theta})$. This field determines which attribute *attends* to which position in space $\mathbf{x}$:

$$\mathbf{m}_0(\mathbf{x}) \oplus \mathbf{m}(\mathbf{x}) = \mathcal{M}(\mathcal{K}(\mathbf{x}), \boldsymbol{\beta}(\mathbf{x}), \boldsymbol{\alpha}(\mathbf{x}); \boldsymbol{\theta}), \tag{16}$$

$$\mathcal{M} : \mathbb{R}^3 \times \mathbb{R}^B \times \mathbb{R}^{A \times d} \rightarrow \mathbb{R}_+^{A+1}, \tag{17}$$

where $\oplus$ is a concatenation operator, $\mathbf{m}(\mathbf{x})$=$\{\mathbf{m}_a(\mathbf{x})\}$, and the additional mask $\mathbf{m}_0(\mathbf{x})$ denotes space that is not affected by *any* attribute. Note that because the mask location should be affected by both the particular attribute of interest (*e.g.*, the selected eye status) and the global appearance of the scene (*e.g.*, head movement), $\mathcal{M}$ takes both $\boldsymbol{\beta}(\mathbf{x})$ and $\boldsymbol{\alpha}(\mathbf{x})$ as input in addition to $\mathcal{K}(\mathbf{x})$. In addition, because the mask is modeling the attention related to attributes, collectively, these masks satisfy the partition of unity property:

$$\mathbf{m}_0(\mathbf{x}) + \Sigma_a[\mathbf{m}_a(\mathbf{x})] = 1 \quad \forall \mathbf{x} \in \mathbb{R}^3. \tag{18}$$

Finally, in a similar spirit to Eq. (5), all of this information is processed by a neural network that produces the desired radiance and density fields used in volume rendering:

$$\left.\begin{matrix}\mathbf{c}(\mathbf{x}) \\ \sigma(\mathbf{x})\end{matrix}\right\} = \mathcal{R}(\mathcal{K}(\mathbf{x}), \underbrace{\mathbf{m}(\mathbf{x}) \odot \boldsymbol{\alpha}(\mathbf{x})}_{\text{attribute controls}}, \underbrace{\mathbf{m}_0(\mathbf{x}) \cdot \boldsymbol{\beta}(\mathbf{x})}_{\text{everything else}}; \boldsymbol{\theta}). \tag{19}$$

In particular, note that $\mathbf{m}(\mathbf{x})=0$ implies $\mathbf{m}_0(\mathbf{x})=1$, hence our solution has the capability of reverting to classical HyperNeRF Eq. (5), where all change in the scene is globally encoded in $\boldsymbol{\beta}(\mathbf{x})$. Finally, these fields can be used to render the mask in image space, following a process analogous to volume rendering of radiance:

$$\mathbf{M}(\mathbf{r}; \boldsymbol{\theta}) = \int_{t_n}^{t_f} T(t) \cdot \sigma(\mathbf{r}(t)) \cdot [\mathbf{m}_0(\mathbf{r}(t)) \oplus \mathbf{m}(\mathbf{r}(t))]\, dt. \tag{20}$$

We depict our inference flow in Fig. 3 (b).

3.4.4 Implementation details

We implement our method for NeRF based on the JAX [6] implementation of HyperNeRF [58]. We use both the scheduled windowed positional encoding and weight initialization of [56], as well as the coarse-to-fine training strategy [58].

Besides the newly added networks, we follow the same architecture as HyperNeRF. For the attribute network $\mathcal{A}$ we use a six-layer multi-layer perceptron (MLP) with 32 neurons at each layer, with a skip connection at the fifth layer, following [56, 58]. For the lifting network $\mathcal{H}_a$, we use the same architecture as $\mathcal{H}$, except for the input and output dimension sizes. For the masking network $\mathcal{M}$ we use a four-layer MLP with 128 neurons at each layer, followed by an additional 64 neuron layer with a skip connection. The network $\mathcal{R}$ also shares the same architecture as HyperNeRF, but with a different input dimension size to accommodate for the changes our method introduces.

2D implementation To show that our idea is not limited to neural radiance fields, we also test a 2D version of our framework that can be used to directly represent images, without going through volume rendering. We use the same architecture and training procedure as in the NeRF case, with the exception that we do not predict the density σ, and we also do not have the notion of depth—each ray is directly the pixel. We center crop each video and resize each frame to be 128×128.

Hyperparameters We train all our NeRF models with 480×270 images and with 128 samples per ray. We train for 250k iterations with a batch size of 512 rays. During training, we maintain that 10% of rays are sampled from annotated images. We set $\mathcal{L}_{\text{attr}} = 10^{-1}$, $\mathcal{L}_{\text{mask}} = 10^{-2}$ and $\mathcal{L}_{\text{enc}} = 10^{-4}$. For the number of hyper dimensions we set $d = 8$. For the 2D implementation

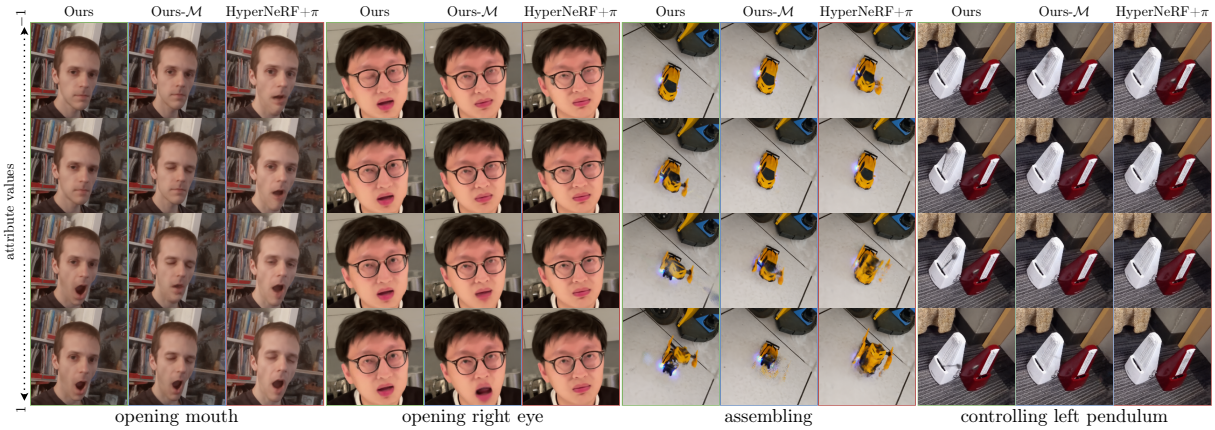

Figure 4. Novel view and novel attribute synthesis on real data – We synthesize scenes from a novel view and with a novel attribute combination, not seen during training. A naive extension of HyperNeRF, HyperNeRF+π fails to disentangle attributes and results in a modification of the scene irrespectively of attribute meaning *e.g.*, opening mouth results in closing eyes at the same time. Ours-$\mathcal{M}$ improves the results, but does not disentangles the attribute space, as successfully done by our complete method. The differences between these methods can even lead to complete failure cases, as shown in the metronome and the toy car case.

experiments, we sample 64 random images from the scene and further subsample 1024 pixels from each of them. For all experiments we use Adam [37] with learning rate 10^{-4} exponentially decaying to 10^{-5} in 250k iterations. We provide additional details in the supplementary material. Training a single model takes around 12 hours on an NVIDIA V100 GPU.

3.5 Results

3.5.1 Datasets and baselines

We evaluate our method on two datasets: real video sequences captured with a smartphone (*real dataset*) and synthetically rendered sequences (*synthetic dataset*). Here we introduce those datasets and the baselines for our approach.

Real dataset Each of the seven real sequences is 1 minute long and was captured either with a Google Pixel 3a or an Apple iPhone 13 Pro. Four of them consists of people performing different facial expressions including smiling, frowning, closing or opening eyes, and opening mouth. For the other three, we captured a toy car changing its shape (*a.k.a.* Transformer), a single metronome, and two metronomes beating with different rates. For one of the four videos depicting people, to use it for the 2D implementation case, we captured it with a static camera that shows a frontal view of the person. All other sequences feature camera motions showing front and sides of the object in the center of the scene. For videos with human subjects, the subjects signed a participant consent form, which was approved by a research ethics board. We informed the participants that their data will be altered with our method.

We extract frames at 15 FPS which gives approximately 900 frames per capture. Because novel attribute synthesis via user control on real scenes does not have a ground truth view—we aim to create scenes with unseen attribute combinations—the benefit of our method is best seen qualitatively. Nonetheless, to quantitatively evaluate the rendering quality, we interpolate between two frames and evaluate its quality. In more detail, to minimize the chance of the dynamic nature of the scene interfering with this assessment, we use every other frame as a test frame for the interpolation task.

For all human videos, we define three attributes—one for the status of each of the two eyes, and one for the mouth. We annotate only six frames per video in this case, specifically the frames that contain the extremes of each attribute (*e.g.*, left eye fully open). For the toy car, we set the shape of the toy car to be an attribute, and annotate two extremes from two different view points—when the toy is in robot-mode and when it is in car-mode from its left and right side. For the metronomes, we consider the state of the pendulum to be the attribute and annotate the two frames with the two extremes for the single metronome case, and seven frames for the two metronome case as the pendulums of the two metronomes are often close to each other and required special annotations for these close-up cases; see Fig. 4.

Synthetic dataset Since the lack of ground-truth data renders measuring the quality of novel attribute synthesis infeasible in practice, we leverage Kubric software [21] to generate synthetic dataset, where we know exactly the state of each object in the scene. We create a simple scene where three 3D objects, the teapot [74], the Stanford bunny [7], and Suzanne [72], are placed within the scene and are rendered with varying surface colors, which are our attributes; see Fig. 6. We generate 900 frames for training and 900 frames for testing. To ensure that the attribute combination during training is not seen in the test scene, we set the attributes to be synchronized for the training split, and desynchronized for the test split. We further render the test split from different camera positions than the training split to account for novel views. We randomly sample 5% of the frames with a given attribute for each object to be set as the ground-truth attribute. During validation, we use attribute values directly to predict the image.

Baselines To evaluate the reconstruction quality of our method, CoNeRF, we compare it with four different baselines: ① standard NeRF [49]; ② NeRF+Latent, a simple extension to NeRF where we concatenate each coordinate $\mathbf{x}$ with a learnable latent code $\boldsymbol{\beta}$ to support appearance changes of the scene; ③ Nerfies [56]; and ④ HyperNeRF[2] [58]. Additionally, as existing methods do not support attribute-based control with a few-shot supervision, we create another baseline ⑤ by extending HyperNeRF with a simple linear regressor π that regresses $\boldsymbol{\beta}_c$ given $\boldsymbol{\alpha}_c$. We call this baseline HyperNeRF+π. To further show the importance of masking, we also compare our approach against a stripped-down version of our method, Ours-$\mathcal{M}$, where we disable the part

[2]We use the version with dynamic plane slicing as it consistently outperforms the axis-aligned strategy; see [58] for more details.

(a) annotation **(b)** unannotated views

Figure 5. Annotation example – We provide only a rough annotation for each attribute, which is enough for the method to discover the mask for each attribute across all views automatically. Bottom row shows masks overlaid on the image.

of our pipeline responsible for masking. All baselines that utilize annotations were trained with the same sparse labels as our method.

3.5.2 Comparison with the baselines

Qualitative highlights We first show qualitative examples of novel attribute and view synthesis on the real dataset in Fig. 4. Our method allows for controlling the selected attribute without changing other aspects of the image—our control is disentangled. This disentanglement allows our method to generate images with attribute combinations that were not seen at training time. On the contrary, as there is no incentive for the learned embeddings of HyperNeRF to be disentangled, the simple regression strategy of HyperNeRF+π results in entangled control, where when one tries to close/open the mouth it ends up affecting the eyes. The same phenomenon happens also for Ours-$\mathcal{M}$. Moreover, due to the complexity of motions in the scene, HyperNeRF+π fails completely to render novel views of the toy car, whereas our method, with only four annotated frames, successfully provides both controllability and high-quality renderings. Please also see `Supplementary` for more qualitative results, including a video demonstration.

Note that in all of these sequences, we provide highly sparse annotations and yet our method learns how each attribute should influence the appearance of the scene. In Fig. 5, we show an example annotation and how the method finds the mask for unannotated views.

Quantitative results on synthetic dataset To complete the qualitative evaluation of our method, we provide results using synthetic dataset with available ground truth. We measure Peak Signal-to-Noise Ratio (PSNR), Multi-scale Structural Similarity (MS-SSIM) [79], and Learned Perceptual Image Patch Similarity (LPIPS) [88] and report them in Tab. 1. With only

Method	PSNR↑	MS-SSIM↑	LPIPS↓
HyperNeRF+π	25.963	0.854	0.158
Ours-$\mathcal{M}$	27.868	0.898	0.155
Ours	**32.394**	**0.972**	**0.139**

Table 1. Novel view and novel attributes results – We report average PSNR, MS-SSIM, and LPIPS values for novel view and novel attribute synthesis on synthetic data. Our method gives the best results.

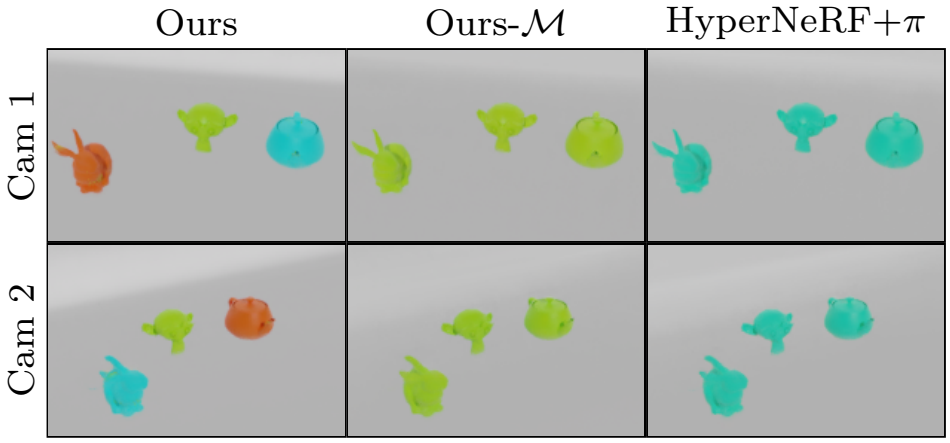

Figure 6. Novel view and novel attribute synthesis on synthetic data – We show examples of novel view and novel attribute synthesis on synthetic data. The scene is composed of three objects, where the color of each object is their attribute. Our method provides control over the color of each object independently, whereas both HyperNeRF+π and Ours-$\mathcal{M}$ fail to deliver controllability and results in all three objects having the same attribute in the rendered scene.

Method	PSNR ↑	MS-SSIM ↑	LPIPS ↓
NeRF	28.795	0.951	0.210
NeRF + Latent	32.653	0.981	0.182
NeRFies	32.274	0.981	0.180
HyperNeRF	32.520	0.981	0.169
Ours-$\mathcal{M}$	32.061	0.979	0.167
Ours	32.342	0.981	0.168

Table 2. Quantitative results (interpolation) – We report results in terms of PSNR, MS-SSIM, and LPIPS for the interpolation task. These results are obtained for interpolated view synthesis only, not for novel attribute rendering. Our method provides similar performance in terms of rendering quality, but with controllability.

5% of the annotations, our method provides the best novel-view and novel-attribute synthesis results, as reconfirmed by the qualitative examples in Tab. 1. As shown, neither HyperNeRF+π nor Ours-$\mathcal{M}$ is able to provide good results in this case, as without disentangled control of each attribute, the novel attribute and view settings of each test frame cannot be synthesized properly.

Interpolation task To further verify that our rendering quality does not degrade with the introduction of controllability, we evaluate our method on a frame interpolation task without any attribute control. Unsurprisingly, as shown in Tab. 2, all methods that support dynamic scenes work similarly, including ours for interpolation. Note that for the interpolation task, we interpolate every other frame, in order to minimize the chance of attributes affecting the evaluation. Here, we are purely interested in the rendering quality from a novel view.

3.5.3 Direct 2D rendering

To verify how our approach generalizes beyond NeRF models and volume rendering, we apply our method to videos taken from a single view point, creating a 2D rendering task. We show in Fig. 7 a proof-of-concept for employing our approach outside of NeRF applications to allow controllable neural generative models.

3.5.4 Ablation study

Loss functions In Tab. 3, we show how each loss term affects the network's performance, contributing to performance improvements. When rendering novel views with novel attributes, the full formulation is a must, as without all loss terms the performance drops significantly—for example, results without $\mathcal{L}_{\text{mask}}$ is similar to Ours-$\mathcal{M}$ results in Tab. 1 and Fig. 6. In the case of the interpolation task, the additional loss functions for controllability have no significant effect on the rendering quality. In other words, our controllability losses **do not interfere** with the rendering quality, other than imbuing the framework with controllability.

Figure 7. 2D image generation example – Our framework also generalizes to direct generation of 2D images. Here we show novel attribute synthesis for a webcam video of a person making expressions. Each individual part of the scene is correctly controlled according to the attribute values.

	Real (interpolation)			Synthetic (novel view & attr.)		
Model	PSNR ↑	MS-SSIM ↑	LPIPS ↓	PSNR ↑	MS-SSIM ↑	LPIPS ↓
Base ($\mathcal{L}_{\text{recon}}$)	32.457	0.981	0.168	24.407	0.718	0.173
$+\mathcal{L}_{\text{enc}}$	32.478	0.982	0.167	27.018	0.871	0.164
$+\mathcal{L}_{\text{enc}} + \mathcal{L}_{\text{attr}}$	32.254	0.981	0.167	27.322	0.873	0.147
$+\mathcal{L}_{\text{enc}} + \mathcal{L}_{\text{attr}} + \mathcal{L}_{\text{mask}}$	32.342	0.981	0.168	**32.394**	**0.972**	**0.139**

Table 3. Effect of loss functions – We report the rendering quality of our method as we procedurally introduce the loss terms. For controlled rendering with novel views and attributes (synthetic data), each loss term adds to the rendering quality, with the $\mathcal{L}_{\text{mask}}$ being critical. For the novel view rendering on real data, addition of loss functions for controllability do not have a significant effect on the rendering quality—they do no harm.

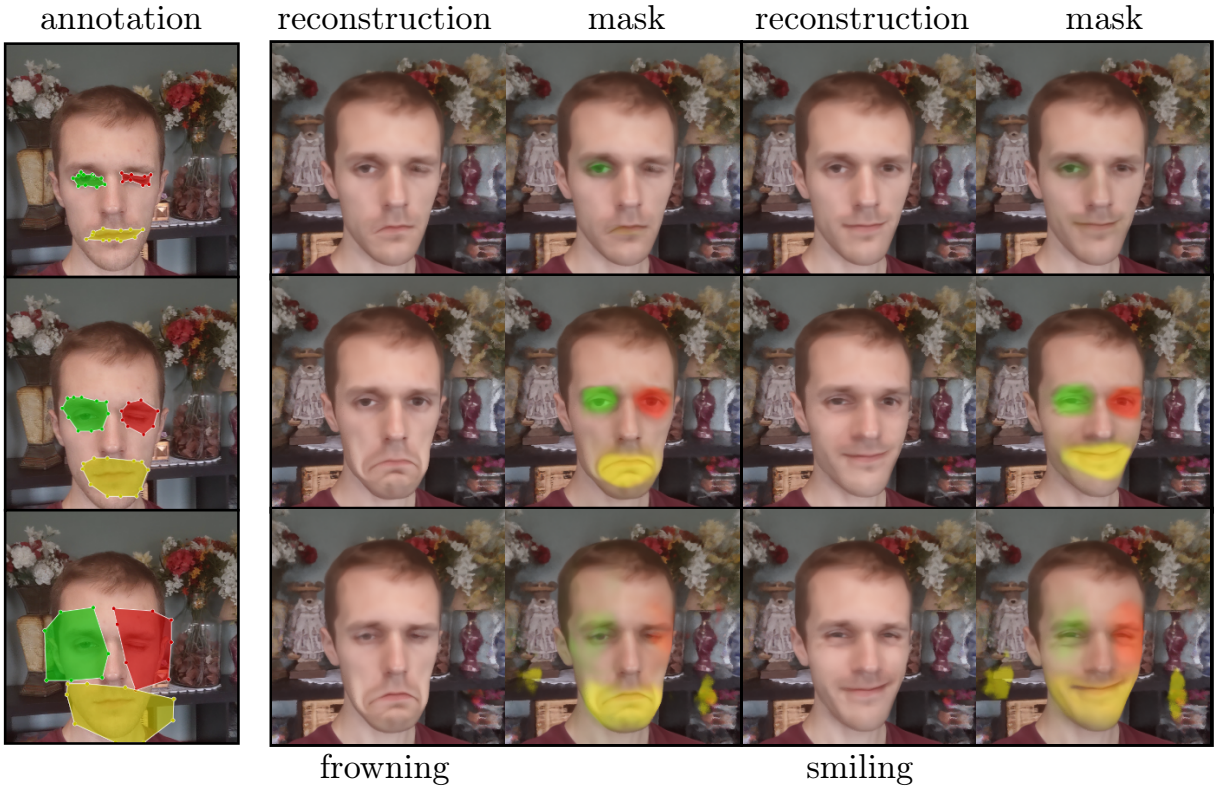

Figure 8. Effect of annotation quality – Our method is moderately robust to the quality of annotations. We visualize the results for two expressions: frowning and smiling, while keeping both eyes in a neutral position. Even with wildly varying annotations as shown, the reconstructions are reasonably controlled, with the exception of the top row, where we show a case where the annotations is too restrictive, resulting in the annotation being ignored for one eye. We show in bottom row also an interesting case, where the mask is large enough to start capturing the correlation among mouth expressions and the eye.

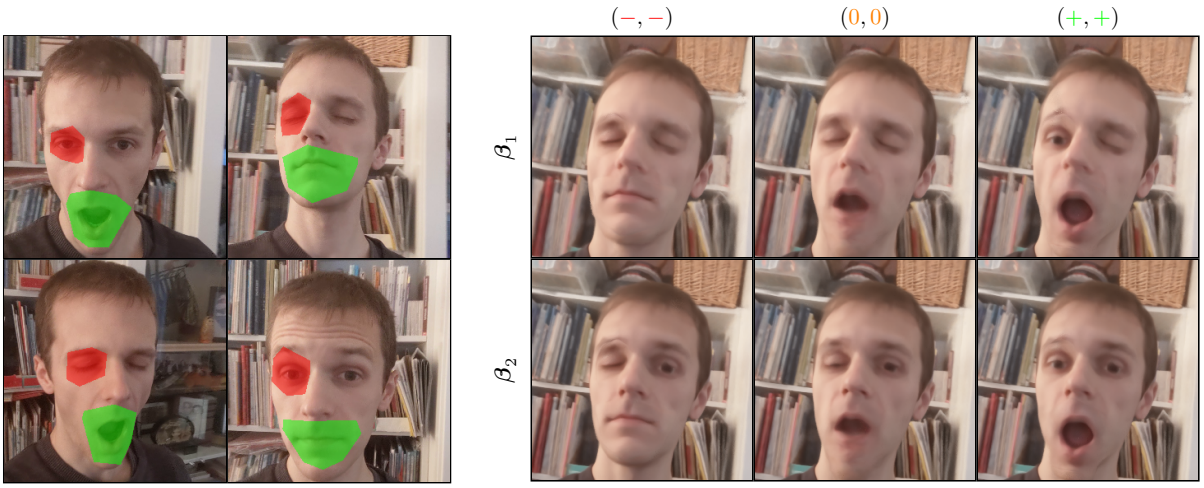

(a) annotated samples **(b)** renderings

Figure 9. Example with unannotated attributes – We show an example of how our method performs when a part of the image changes appearance, but is not annotated. With the annotations in (a), we synthesize the scene with novel view and attributes in (b), where the two rows are with different $\boldsymbol{\beta}$ configurations. We denote the attribute configuration on the top of each column in (b). As shown, the change that is not annotated is simply encoded in the per-image encoding $\boldsymbol{\beta}$.

Quality of few shot supervision We test how sensitive our method is against the quality of annotation supervision. In Fig. 8 we demonstrate how each annotation leads to the final rendering quality. Our framework is robust to a moderate degree to the inaccuracies in the annotations. However, when they are too restrictive, the mask may collapse, as shown on the top row. Too large of a mask could also lead to moderate entanglement of attributes, as shown in the bottom row. Still, in all cases, our method provides a reasonable control over what is annotated.

Unannotated attributes A natural question to ask is then what happens with the unannotated changes that may exist in the scene. In Fig. 9 we show how the method performs when annotating only parts of the appearance change within the scene. The unannotated changes of the scene get encoded as $\boldsymbol{\beta}$, as in the case of HyperNeRF [58].

3.6 Conclusions

We have introduced CoNeRF, an intuitive controllable NeRF model that can be trained with few-shot annotations in the form of attribute masks. The core contribution of our method is that we represent attributes as localized masks, which are then treated as latent variables within the framework. To do so we regress the attribute and their corresponding masks with neural networks. This leads to a few-shot learning setup, where the network learns to regress provided annotations, and if they are not provided for a given image, proper attributes and masked are

discovered throughout training automatically. We have shown that our method allows users to easily annotate what to control and how, within a single video simply by annotating a few frames, which then allows rendering of the scene from novel views and with novel attributes, at high quality.

Limitations While our method delivers controllability to NeRF models, there is room for improvement. First, our disentanglement of attribute strictly relies on the locality assumption—if multiple attributes act on a single pixel, our method is likely to have entangled outcomes when rendering with different attributes. An interesting direction would therefore be to incorporate manifold disentanglement approaches [40, 89] to our method. Second, while very few, we still require sparse annotations. Unsupervised discovery of controllable attributes, for example as in [38], in a scene remains yet to be explored. Lastly, we resort to user intuition on which frames should be annotated—we heuristically choose frames with extreme attributes (*e.g.*, mouth fully open). While this is a valid strategy, an interesting direction for future research would be to employ active learning techniques for this purpose [4, 63]

We further discuss potential societal impact of our work in the `Supplementary`.

3.7 Acknowledgements

We thank Thabo Beeler, JP Lewis, and Mark J. Matthews for their fruitful discussions, and Daniel Rebain for helping with processing the synthetic dataset. The work was partly supported by National Sciences and Engineering Research Council of Canada (NSERC), Compute Canada, and Microsoft Mixed Reality & AI Lab. This research was funded by Foundation for Polish Science (grant no POIR.04.04.00-00-14DE/18-00 carried out within the Team-Net program co-financed by the European Union under the European Regional Development Fund), National Science Centre, Poland (grant no 2020/39/B/ST6/01511), and by Microsoft Research through EMEA PhD Scholarship Programme. The authors have applied a CC BY license to any Author Accepted Manuscript (AAM) version arising from this submission, in accordance with the grants' open access conditions.

CoNeRF: Controllable Neural Radiance Fields

Supplementary Material

3.8 Potential social impact

Our work is originally intended for creative and entertainment purposes, for example to allow users to easily edit their personal photos to have all the members of a group photo to have

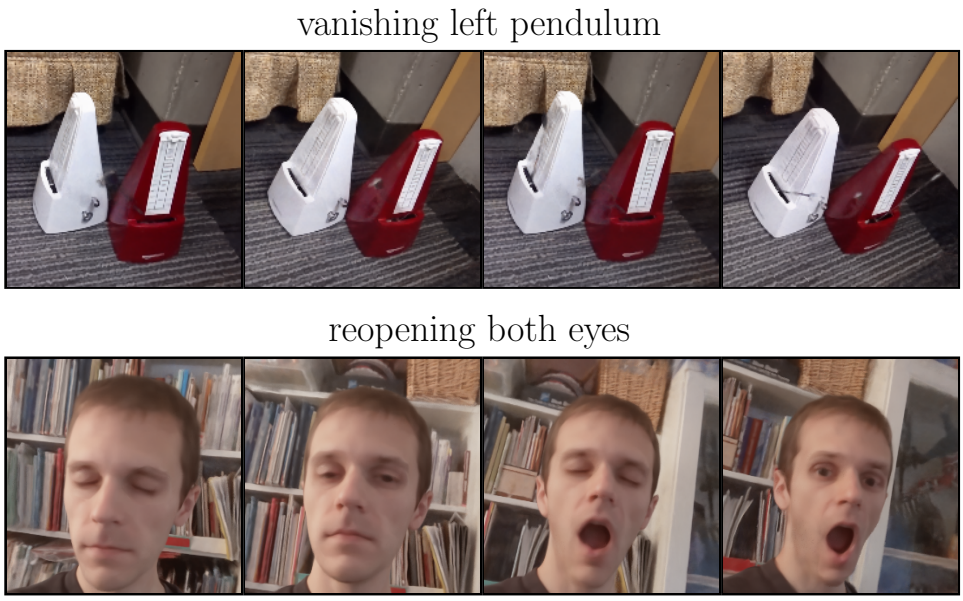

Figure 10. Failure cases – Our model may learn spurious interpolations for controlled elements that occupy little space in the image and with insufficient/careless annotations. For the metronome, due to the fast motion of the pendulum and its specularity, without careful annotation our method may simply learn its motion blur or sometimes even completely ignore the pendulum. In the face example, this may result in the eye blinking multiple times while interpolating between the attribute values of -1 and 1. Both cases are preventable with more careful annotations and by annotating more frames.

their eyes open. However, as with all work that enable editable models, our method has the potential to be misused for malicious purposes such as deep fakes. We strongly advise against such misuse. Recent work [3] has shown that it is possible to detect deep fakes, hinting that it should be possible to detect these deep learning-generated images. One of our future research direction is also along these lines, where we now aim to reliably detect images generated by our method.

3.9 Architecture details

We present architecture of: canonicalizer $\mathcal{K}$ in Fig. 11, attribute map $\mathcal{A}$ in Fig. 12, hypermap $\mathcal{H}$ in Fig. 13, per-attribute hypermap in Fig. 14, mask prediction network in Fig. 15 and the rendering network in Fig. 16. Each network contains only fully connected layers. Hidden layers use ReLU activation function. Colors of figures correspond to colors of blocks in Fig. 3b.

3.10 Failure Cases

We identify two modes of failure cases in our approach and present them in Fig. 10. In some cases with particular mask annotations, our model can struggle with controlling elements that occupy small space in the image. The problem is especially visible for controlling pendulum

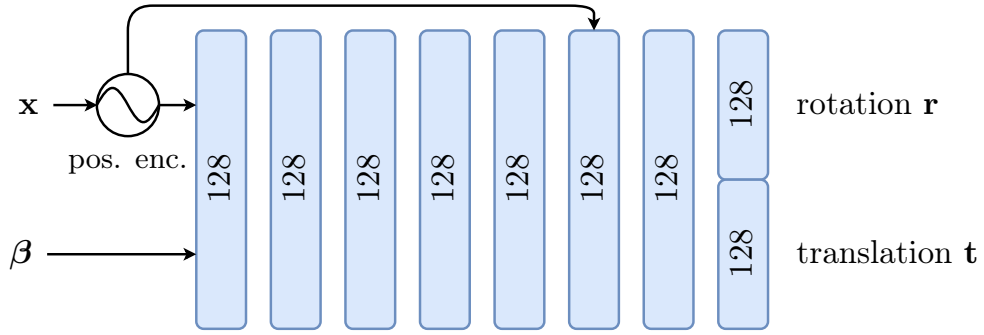

Figure 11. The canonicalization network takes positionally encoded raw coordinates $\mathbf{x}$ and learnable per-image latent code $\boldsymbol{\beta}$ and outputs rotation $\mathbf{r}$ expressed as a quaternion and translation $\mathbf{t}$. We rigidly transform each point $\mathbf{x}$ with an affine transform using both output. We use windowed positional encoding [56] for $\mathbf{x}$ with 8 components, linearly increasing contribution of components throughout 80k steps. We initialize the last layer to small values so the network can learn a base structure of the data.

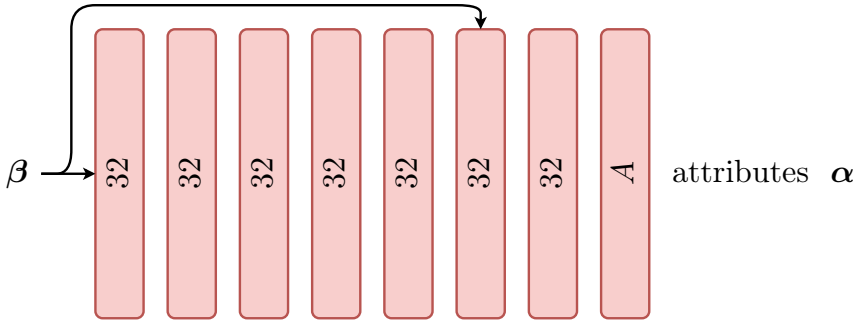

Figure 12. The attribute map $\mathcal{A}$ takes a per-image learnable latent code $\boldsymbol{\beta}$ and outputs A attributes $\boldsymbol{\alpha}$.

movement or opening and closing eyes. In the former, pendulum disappears and reappears in different places. In the latter, the control of eyes is periodic and there are two distant values in $[-1, 1]$ that produce opening eyes. While with careful annotations we noticed that the problem is mostly preventable, this problem may occur in practice.

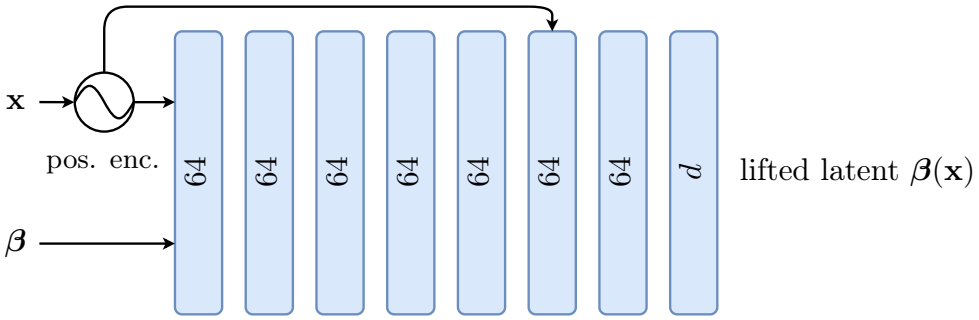

Figure 13. The network predicting lifted latent code $\boldsymbol{\beta}$, takes per-image $\boldsymbol{\beta}$ as an input, positionally encoded raw points $\boldsymbol{\beta}$ and outputs a lifted code of size d. We use only one sine component to encode $\mathbf{x}$.

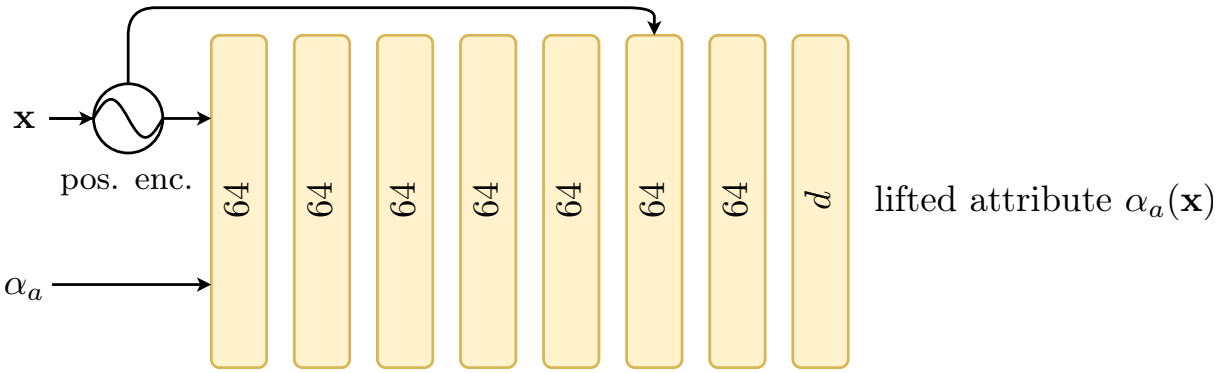

Figure 14. Per-attributes hypermaps take an attribute together with encoded $\mathbf{x}$ coordinates and output lifted $\alpha_a(\mathbf{x})$ ambient code of size d. We encode $\mathbf{x}$ with only single component.

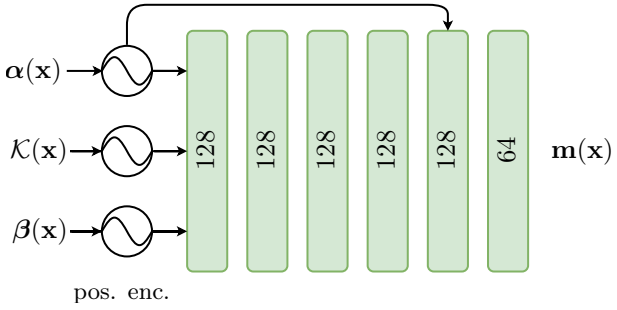

Figure 15. Masking network $\mathcal{M}$ take lifted attributes $\boldsymbol{\alpha}(\mathbf{x})$, lifted latent code $\boldsymbol{\beta}(\mathbf{x})$ and canonicalized points $\mathcal{K}(\mathbf{x})$. We transform $\boldsymbol{\alpha}(\mathbf{x})$ and $\boldsymbol{\beta}(\mathbf{x})$ through a windowed positional encoding where we start at 1k-th step linearly increasing a single sine component for the next 10k steps. Points $\mathcal{K}(\mathbf{x})$ are encoded with 8 components. The output is activated with a sigmoid function. We realize $\mathbf{m}_0(\mathbf{x})$ as $\mathbf{m}(\mathbf{x})_0 = 1 - \sum_{a \in A} \mathbf{m}_a(\mathbf{x})$, and clip the output to ensure the values range to be in $[0, 1]$. Note that while the network shares similarities with the radiance field prediction part $\mathcal{R}$, it is not conditioned on view directions and appearance codes.

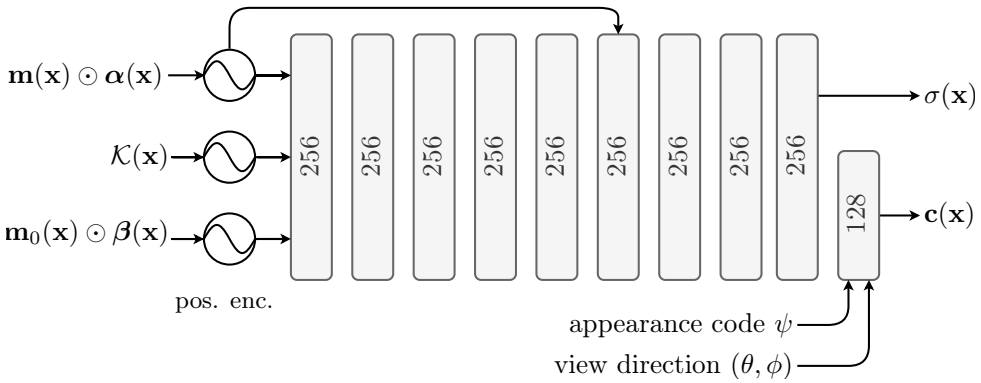

Figure 16. The radiance field prediction network predicts RGB colors $\mathbf{c}(\mathbf{x})$ and density values $\sigma(\mathbf{x})$ from canonicalized points. We encode points $\mathbf{x}$ with 8 sine components and linearly increase contribution of a single component in $\boldsymbol{\alpha}(\mathbf{x})$ and $\boldsymbol{\beta}(\mathbf{x})$ from 1k to 11k step. Per-point predicted predicted attributes $\boldsymbol{\alpha}(\mathbf{x})$ and lifted latent code $\boldsymbol{\beta}(\mathbf{x})$ are masked by a mask predicted from the masking network depicted in Fig. 15. The final linear layer takes additional per-image learnable appearance code ψ to account for any visual variations that cannot be explained by the rest of the framework (*e.g.* changes in lighting). The code can discarded during evaluation. The same layer is additionally conditioned on the positionally encoded view directions. We activate the color output with a sigmoid function.

Chapter 4

Final remarks and discussion

4.1 Conclusions

4.2 Future work

Bibliography

[1] Agarwala, A., Dontcheva, M., Agrawala, M., Drucker, S., Colburn, A., Curless, B., Salesin, D., and Cohen, M., "Interactive Digital Photomontage," in *ACM SIGGRAPH 2004 Papers*, ser. SIGGRAPH '04, Los Angeles, California: Association for Computing Machinery, 2004, pp. 294–302, ISBN: 9781450378239. DOI: 10.1145/1186562.1015718. [Online]. Available: https://doi.org/10.1145/1186562.1015718 (cit. on p. 16).

[2] Alldieck, T., Xu, H., and Sminchisescu, C., "imGHUM: Implicit Generative Models of 3D Human Shape and Articulated Pose," in *CVPR*, 2021 (cit. on p. 18).

[3] Asnani, V., Yin, X., Hassner, T., and Liu, X., "Reverse Engineering of Generative Models: Inferring Model Hyperparameters from Generated Images," 2021 (cit. on p. 32).

[4] Belharbi, S., Ben Ayed, I., McCaffrey, L., and Granger, E., "Deep Active Learning for Joint Classification & Segmentation with Weak Annotator," 2021 (cit. on p. 31).

[5] Blanz, V. and Vetter, T., "A Morphable Model For The Synthesis Of 3D Faces," in *CGIT*, 1999, pp. 187–194 (cit. on p. 16).

[6] Bradbury, J., Frostig, R., Hawkins, P., Johnson, M. J., Leary, C., Maclaurin, D., Necula, G., Paszke, A., VanderPlas, J., Wanderman-Milne, S., and Zhang, Q., *JAX: Composable Transformations of Python+NumPy Programs*, http://github.com/google/jax, version 0.2.5, 2018 (cit. on p. 22).

[7] *Bunny 3D model*, https://graphics.stanford.edu/~mdfisher/Data/Meshes/bunny.obj, Accessed: 2021-11-16 (cit. on p. 24).

[8] Cao, C., Simon, T., Kim, J. K., Schwartz, G., Zollhoefer, M., Saito, S.-S., Lombardi, S., Wei, S.-E., Belko, D., Yu, S.-I., *et al.*, "Authentic Volumetric Avatars from a Phone Scan," *ToG*, vol. 41, no. 4, pp. 1–19, 2022 (cit. on p. 7).

[9] Chen, X., Duan, Y., Houthooft, R., Schulman, J., Sutskever, I., and Abbeel, P., "InfoGAN: Interpretable Representation Learning by Information Maximizing Generative Adversarial Nets," in *NeurIPS*, 2016 (cit. on p. 16).

[10] Chen, X., Zhang, Q., Li, X., Chen, Y., Feng, Y., Wang, X., and Wang, J., "Hallucinated Neural Radiance Fields in the Wild," in *CVPR*, 2022, pp. 12 943–12 952 (cit. on p. 7).

[11] Deng, B., Lewis, J. P., Jeruzalski, T., Pons-Moll, G., Hinton, G., Norouzi, M., and Tagliasacchi, A., "NASA: Neural Articulated Shape Approximation," in *ECCV*, 2020 (cit. on p. 18).

[12] Ekman, P. and Rosenberg, E. L., *What the Face Reveals: Basic and Applied Studies of Spontaneous Expression Using the Facial Action Coding System (FACS)*. Oxford University Press, USA, 1997 (cit. on p. 16).

[13] Esposito, S., Xu, Q., **Kania**, **K.**, Hewitt, C., Mariotti, O., Petikam, L., Valentin, J., Onken, A., and Mac Aodha, O., "GeoGen: Geometry-Aware Generative Modeling via Signed Distance Functions," in *CVPRW*, 2024, pp. 7479–7488 (cit. on p. 12).

[14] Fang, J., Yi, T., Wang, X., Xie, L., Zhang, X., Liu, W., Nießner, M., and Tian, Q., "Fast Dynamic Radiance Fields with Time-Aware Neural Voxels," in *SIGGRAPH Asia 2022 Conference Papers*, 2022, pp. 1–9 (cit. on p. 6).

[15] Feng, Y., Feng, H., Black, M. J., and Bolkart, T., "Learning an Animatable Detailed 3D Face Model from In-The-Wild Images," *ToG*, vol. 40, no. 4, pp. 1–13, 2021 (cit. on p. 6).

[16] Gafni, G., Thies, J., Zollhofer, M., and Nießner, M., "Dynamic Neural Radiance Fields for Monocular 4d Facial Avatar Reconstruction," in *CVPR*, 2021, pp. 8649–8658 (cit. on pp. 15, 17).

[17] Garbin, S. J., Kowalski, M., Estellers, V., Szymanowicz, S., Rezaeifar, S., Shen, J., Johnson, M. A., and Valentin, J., "VolTeMorph: Real-time, Controllable and Generalizable Animation of Volumetric Representations," in *CGS*, Wiley Online Library, vol. 43, 2024, e15117 (cit. on pp. 7, 8, 10).

[18] Garbin, S. J., Kowalski, M., Johnson, M., Shotton, J., and Valentin, J., "FastNeRF: High-Fidelity Neural Rendering at 200FPS," in *ICCV*, 2021, pp. 14 346–14 355 (cit. on p. 7).

[19] Grassal, P.-W., Prinzler, M., Leistner, T., Rother, C., Nießner, M., and Thies, J., "Neural Head Avatars From Monocular RGB Videos," in *CVPR*, 2022, pp. 18 653–18 664 (cit. on p. 6).

[20] Green, R., "Spherical harmonic lighting: The gritty details," in *Archives of the game developers conference*, vol. 56, 2003, p. 4 (cit. on p. 11).

[21] Greff, K., Tagliasacchi, A., Liu, D., and Laradji, I., *Kubric*, `http://github.com/google-research/kubric`, version 0.1.1, 2021 (cit. on p. 24).

[22] Guo, M., Fathi, A., Wu, J., and Funkhouser, T., "Object-Centric Neural Scene Rendering," 2020 (cit. on p. 17).

[23] He, T., Xu, Y., Saito, S., Soatto, S., and Tung, T., "ARCH++: Animation-Ready Clothed Human Reconstruction Revisited," in *ICCV*, 2021 (cit. on p. 18).

[24] Hedman, P., Srinivasan, P. P., Mildenhall, B., Barron, J. T., and Debevec, P., "Baking Neural Radiance Fields for Real-Time View Synthesis," in *ICCV*, 2021, pp. 5875–5884 (cit. on p. 7).

[25] Higgins, I., Amos, D., Pfau, D., Racaniere, S., Matthey, L., Rezende, D., and Lerchner, A., "Towards a Definition of Disentangled Representations," 2018 (cit. on p. 16).

[26] Higgins, I., Matthey, L., Pal, A., Burgess, C., Glorot, X., Botvinick, M., Mohamed, S., and Lerchner, A., "beta-VAE: Learning Basic Visual Concepts with a Constrained Variational Framework," in *ICLR*, 2017 (cit. on p. 16).

[27] Huang, B., Yu, Z., Chen, A., Geiger, A., and Gao, S., "2D Gaussian Splatting for Geometrically Accurate Radiance Fields," in *ACM SIGGRAPH 2024 Conference Papers*, 2024, pp. 1–11 (cit. on pp. 7, 8, 11).

[28] Jang, W. and Agapito, L., "CodeNeRF: Disentangled Neural Radiance Fields for Object Categories," in *ICCV*, 2021 (cit. on pp. 15, 17).

[29] Kajiya, J. T. and Von Herzen, B. P., "Ray Tracing Volume Densities," *ACM SIGGRAPH Computer Graphics*, vol. 18, no. 3, pp. 165–174, 1984 (cit. on p. 18).

[30] Kaleta, J., Kania, K., Trzcinski, T., and Kowalski, M., "LumiGauss: High-Fidelity Outdoor Relighting with 2D Gaussian Splatting," 2025 (cit. on pp. 8, 11, 12).

[31] Kania, K., Garbin, S. J., Tagliasacchi, A., Estellers, V., Yi, K. M., Valentin, J., Trzciński, T., and Kowalski, M., "BlendFields: Few-Shot Example-Driven Facial Modeling," in *CVPR*, 2023, pp. 404–415 (cit. on pp. 7, 8, 10, 12).

[32] Kania, K., Khirodkar, R., Saito, S., Yi, K. M., and Martinez, J., *CLoG: Leveraging UV Space for Continuous Levels of Detail*, 2024 (cit. on pp. 8, 9, 11, 12).

[33] **Kania**, **K.**, Kowalski, M., and Trzciński, T., "TrajeVAE: Controllable Human Motion Generation from Trajectories," *arXiv preprint arXiv:2104.00351*, 2021 (cit. on p. 12).

[34] Kania, K., Yi, K. M., Kowalski, M., Trzciński, T., and Tagliasacchi, A., "CoNeRF: Controllable Neural Radiance Fields," in *CVPR*, 2022 (cit. on pp. 6, 8, 10, 12).

[35] **Kania**, **K.**, Zięba, M., and Kajdanowicz, T., "UCSG-NET – Unsupervised Discovering of Constructive Solid Geometry Tree," *NeurIPS*, vol. 33, pp. 8776–8786, 2020 (cit. on p. 12).

[36] Kerbl, B., Kopanas, G., Leimkühler, T., and Drettakis, G., "3D Gaussian Splatting for Real-Time Radiance Field Rendering," *TOG*, vol. 42, no. 4, pp. 139–1, 2023 (cit. on pp. 5, 7, 9, 11).

[37] Kingma, D. P. and Ba, J., "Adam: A Method for Stochastic Optimization," in *ICLR*, 2015 (cit. on p. 23).

[38] Kulkarni, T., Gupta, A., Ionescu, C., Borgeaud, S., Reynolds, M., Zisserman, A., and Mnih, V., "Unsupervised Learning of Object Keypoints for Perception and Control," in *NeurIPS*, 2019 (cit. on p. 31).

[39] Lewis, J. P., Anjyo, K., Rhee, T., Zhang, M., Pighin, F., and Deng, Z., "Practice and Theory of Blendshape Facial Models," in *Eurographics 2014 - State of the Art Reports*, Lefebvre, S. and Spagnuolo, M., Eds., The Eurographics Association, 2014 (cit. on p. 7).

[40] Li, S. Z., Zang, Z., and Wu, L., "Markov-Lipschitz Deep Learning," 2020 (cit. on p. 31).

[41] Li, T., Bolkart, T., Black, M. J., Li, H., and Romero, J., "Learning a model of facial shape and expression from 4D scans," *SIGGRAPH Asia*, vol. 36, no. 6, 194:1–194:17, 2017 (cit. on p. 10).

[42] Lin, T.-Y., Goyal, P., Girshick, R., He, K., and Dollár, P., "Focal Loss for Dense Object Detection," in *ICCV*, 2017 (cit. on p. 21).

[43] Liu, L., Habermann, M., Rudnev, V., Sarkar, K., Gu, J., and Theobalt, C., "Neural Actor: Neural Free-view Synthesis of Human Actors with Pose Control," 2021 (cit. on pp. 16, 17).

[44] Liu, S., Zhang, X., Zhang, Z., Zhang, R., Zhu, J.-Y., and Russell, B., "Editing Conditional Radiance Fields," in *ICCV*, 2021, pp. 5773–5783 (cit. on pp. 6, 10, 15, 17).

[45] Loper, M., Mahmood, N., Romero, J., Pons-Moll, G., and Black, M., "SMPL: A Skinned Multi-Person Linear Model," *ACM Trans. Graph.*, vol. 34, no. 6, 2015 (cit. on pp. 17, 18).

[46] Ma, Q., Saito, S., Yang, J., Tang, S., and Black, M. J., "SCALE: Modeling Clothed Humans with a Surface Codec of Articulated Local Elements," in *CVPR*, 2021 (cit. on p. 18).

[47] Martin-Brualla, R., Radwan, N., Sajjadi, M. S., Barron, J. T., Dosovitskiy, A., and Duckworth, D., "NeRF in the Wild: Neural Radiance Fields for Unconstrained Photo Collections," in *CVPR*, 2021, pp. 7210–7219 (cit. on pp. 6, 15, 17, 20).

[48] Mihajlovic, M., Zhang, Y., Black, M. J., and Tang, S., "LEAP: Learning Articulated Occupancy of People," in *CVPR*, 2021 (cit. on p. 18).

[49] Mildenhall, B., Srinivasan, P. P., Tancik, M., Barron, J. T., Ramamoorthi, R., and Ng, R., "NeRF: Representing Scenes as Neural Radiance Fields for View Synthesis," *Communications of the ACM*, vol. 65, no. 1, pp. 99–106, 2021 (cit. on pp. 6, 7, 15, 17, 18, 20, 24).

[50] Mu, J., Qiu, W., Kortylewski, A., Yuille, A., Vasconcelos, N., and Wang, X., "A-SDF: Learning Disentangled Signed Distance Functions for Articulated Shape Representation," in *ICCV*, 2021 (cit. on p. 18).

[51] Müller, T., Evans, A., Schied, C., and Keller, A., "Instant Neural Graphics Primitives with a Multiresolution Hash Encoding," *ToG*, vol. 41, no. 4, 102:1–102:15, Jul. 2022 (cit. on p. 7).

[52] Neumann, T., Varanasi, K., Wenger, S., Wacker, M., Magnor, M., and Theobalt, C., "Sparse Localized Deformation Components," *ACM TOG*, vol. 32, no. 6, pp. 1–10, 2013 (cit. on p. 16).

[53] Noguchi, A., Sun, X., Lin, S., and Harada, T., "Neural Articulated Radiance Field," in *ICCV*, 2021 (cit. on p. 17).

[54] Oat, C., "Animated Wrinkle Maps," in *SIGGRAPH*, ser. SIGGRAPH '07, San Diego, California: Association for Computing Machinery, 2007, pp. 33–37, ISBN: 9781450318235 (cit. on pp. 7, 8).

[55] Park, J. J., Florence, P., Straub, J., Newcombe, R., and Lovegrove, S., "DeepSDF: Learning Continuous Signed Distance Functions for Shape Representation," in *CVPR*, 2019 (cit. on pp. 19, 20).

[56] Park, K., Sinha, U., Barron, J. T., Bouaziz, S., Goldman, D. B., Seitz, S. M., and Martin-Brualla, R., "Deformable Neural Radiance Fields," in *ICCV*, 2021 (cit. on pp. 15, 17, 18, 20, 22, 24, 33).

[57] Park, K., Sinha, U., Barron, J. T., Bouaziz, S., Goldman, D. B., Seitz, S. M., and Martin-Brualla, R., "Nerfies: Deformable Neural Radiance Fields," in *ICCV*, 2021, pp. 5865–5874 (cit. on p. 6).

[58] Park, K., Sinha, U., Hedman, P., Barron, J. T., Bouaziz, S., Goldman, D. B., Martin-Brualla, R., and Seitz, S. M., "HyperNeRF: A Higher-Dimensional Representation for Topologically Varying Neural Radiance Fields," *ToG*, vol. 40, no. 6, 2021 (cit. on pp. 6, 10, 15–20, 22, 24, 30).

[59] Patow, G. and Pueyo, X., "A Survey of Inverse Rendering Problems," in *Computer graphics forum*, Wiley Online Library, vol. 22, 2003, pp. 663–687 (cit. on p. 7).

[60] Pumarola, A., Corona, E., Pons-Moll, G., and Moreno-Noguer, F., "D-NeRF: Neural Radiance Fields for Dynamic Scenes," in *CVPR*, 2021, pp. 10 318–10 327 (cit. on p. 6).

[61] Ramamoorthi, R. and Hanrahan, P., "An efficient representation for irradiance environment maps," in *Proceedings of the 28th annual conference on Computer graphics and interactive techniques*, 2001, pp. 497–500 (cit. on pp. 7, 8).

[62] Reiser, C., Peng, S., Liao, Y., and Geiger, A., "KiloNeRF: Speeding Up Neural Radiance Fields With Thousands of Tiny MLPs," in *ICCV*, 2021, pp. 14 335–14 345 (cit. on p. 7).

[63] Ren, P., Xiao, Y., Chang, X., Huang, P.-Y., Li, Z., Chen, X., and Wang, X., "A Survey of Deep Active Learning," 2020 (cit. on p. 31).

[64] Rudnev, V., Elgharib, M., Smith, W., Liu, L., Golyanik, V., and Theobalt, C., "Neural Radiance Fields for Outdoor Scene Relighting," in *European Conference on Computer Vision*, Springer, 2022, pp. 615–631 (cit. on pp. 7, 8).

[65] Saito, S., Yang, J., Ma, Q., and Black, M. J., "SCANimate: Weakly Supervised Learning of Skinned Clothed Avatar Networks," in *CVPR*, 2021 (cit. on p. 18).

[66] Schödl, A. and Essa, I. A., "Controlled Animation of Video Sprites," in *Proceedings of the 2002 ACM SIGGRAPH/Eurographics Symposium on Computer Animation*, ser. SCA '02, San Antonio, Texas: Association for Computing Machinery, 2002, pp. 121–127, ISBN: 1581135734. DOI: 10.1145/545261.545281. [Online]. Available: https://doi.org/10.1145/545261.545281 (cit. on p. 16).

[67] Schwarz, K., Liao, Y., Niemeyer, M., and Geiger, A., "GRAF: Generative Radiance Fields for 3D-Aware Image Synthesis," in *NeurIPS*, 2020 (cit. on p. 17).

[68] Slomp, M. P. B., Oliveira Neto, M. M. d., and Patrício, D. I., "A gentle introduction to precomputed radiance transfer," *Revista de informática teórica e aplicada. Porto Alegre. Vol. 13, n. 2 (2006), p. 131-160*, 2006 (cit. on p. 7).

[69] Spurek, P., Winczowski, S., Zięba, M., Trzciński, T., **Kania**, **K.**, and Mazur, M., "Modeling 3D Surfaces with a Locally Conditioned Atlas," in *ICCS*, Springer, 2024, pp. 100–115 (cit. on p. 12).

[70] Stypułkowski, M., **Kania**, **K.**, Zamorski, M., Zięba, M., Trzciński, T., and Chorowski, J., "Representing Point Clouds with Generative Conditional Invertible Flow Networks," *Pattern Recognition Letters*, vol. 150, pp. 26–32, 2021 (cit. on p. 12).

[71] Su, S.-Y., Yu, F., Zollhöfer, M., and Rhodin, H., "A-NeRF: A-NeRF: Articulated Neural Radiance Fields for Learning Human Shape, Appearance, and Pose," in *NeurIPS*, 2021 (cit. on p. 17).

[72] *Suzanne 3D model*, https://github.com/OpenGLInsights/OpenGLInsightsCode/blob/master/Chapter%2026%20Indexing%20Multiple%20Vertex%20Arrays/article/suzanne.obj, Accessed: 2021-11-16 (cit. on p. 24).

[73] Tancik, M., Srinivasan, P. P., Mildenhall, B., Fridovich-Keil, S., Raghavan, N., Singhal, U., Ramamoorthi, R., Barron, J. T., and Ng, R., "Fourier Features Let Networks Learn High Frequency Functions in Low Dimensional Domains," in *NeurIPS*, 2020 (cit. on pp. 6, 8).

[74] *Teapot 3D model*, https://graphics.stanford.edu/courses/cs148-10-summer/as3/code/as3/teapot.obj, Accessed: 2021-11-16 (cit. on p. 24).

[75] Thies, J., Zollhofer, M., Stamminger, M., Theobalt, C., and Nießner, M., "Face2Face: Real-time Face Capture and Reenactment of RGB Videos," in *CVPR*, 2016 (cit. on p. 17).

[76] Tretschk, E., Tewari, A., Golyanik, V., Zollhöfer, M., Lassner, C., and Theobalt, C., "Non-Rigid Neural Radiance Fields: Reconstruction and Novel View Synthesis of a Dynamic Scene From Monocular Video," in *ICCV*, 2021, pp. 12 959–12 970 (cit. on p. 18).

[77] Trevithick, A. and Yang, B., "GRF: Learning a General Radiance Field for 3D Scene Representation and Rendering," in *ICCV*, 2021 (cit. on p. 17).

[78] Vasconcelos, C. N., Oztireli, C., Matthews, M., Hashemi, M., Swersky, K., and Tagliasacchi, A., "CUF: Continuous Upsampling Filters," in *CVPR*, 2023, pp. 9999–10 008 (cit. on p. 9).

[79] Wang, Z., Simoncelli, E. P., and Bovik, A. C., "Multiscale Structural Similarity for Image Quality Assessment," in *Conference on Signals, Systems & Computers*, 2003 (cit. on p. 25).

[80] Wu, C., Bradley, D., Gross, M., and Beeler, T., "An Anatomically-Constrained Local Deformation Model for Monocular Face Capture," *ACM TOG*, vol. 35, no. 4, pp. 1–12, 2016 (cit. on pp. 16, 17).

[81] Xia, S., Yue, J., **Kania**, **K.**, Fang, L., Tagliasacchi, A., Yi, K. M., and Sun, W., "Densify Your Labels: Unsupervised Clustering with Bipartite Matching for Weakly Supervised Point Cloud Segmentation," *arXiv preprint arXiv:2312.06799*, 2023 (cit. on p. 12).

[82] Xie, C., Park, K., Martin-Brualla, R., and Brown, M., "FiG-NeRF: Figure-Ground Neural Radiance Fields for 3D Object Category Modelling," 2021 (cit. on pp. 6, 17).

[83] Yang, B., Zhang, Y., Xu, Y., Li, Y., Zhou, H., Bao, H., Zhang, G., and Cui, Z., "Learning Object-Compositional Neural Radiance Field for Editable Scene Rendering," in *ICCV*, 2021 (cit. on pp. 15, 17).

[84] Yang, Y., Zhang, S., Huang, Z., Zhang, Y., and Tan, M., "Cross-Ray Neural Radiance Fields for Novel-view Synthesis from Unconstrained Image Collections," in *Proceedings of the IEEE/CVF International Conference on Computer Vision*, 2023, pp. 15 901–15 911 (cit. on p. 7).

[85] Yu, A., Li, R., Tancik, M., Li, H., Ng, R., and Kanazawa, A., "Plenoctrees for Real-time Rendering of Neural Radiance Fields," in *ICCV*, 2021, pp. 5752–5761 (cit. on p. 7).

[86] Yu, H.-X., Guibas, L. J., and Wu, J., "Unsupervised Discovery of Object Radiance Fields," 2021 (cit. on p. 17).

[87] Zhang, K., Riegler, G., Snavely, N., and Koltun, V., "NeRF++: Analyzing and Improving Neural Radiance Fields," 2020 (cit. on pp. 15, 17).

[88] Zhang, R., Isola, P., Efros, A. A., Shechtman, E., and Wang, O., "The Unreasonable Effectiveness of Deep Features as a Perceptual Metric," in *CVPR*, 2018 (cit. on p. 25).

[89] Zhang, S., Moscovich, A., and Singer, A., "Product Manifold Learning," in *Inter. Conf. on Artif. Intell. and Stat.*, 2021 (cit. on p. 31).

[90] Zhang, X., Srinivasan, P. P., Deng, B., Debevec, P., Freeman, W. T., and Barron, J. T., "NeRFactor: Neural Factorization of Shape and Reflectance Under an Unknown Illumination," 2021 (cit. on pp. 10, 15, 17).

[91] Zheng, Z., Yu, T., Liu, Y., and Dai, Q., "PaMIR: Parametric Model-Conditioned Implicit Representation for Image-based Human Reconstruction," *IEEE TPAMI*, 2021 (cit. on p. 18).

[92] Zielonka, W., Bolkart, T., and Thies, J., "Towards Metrical Reconstruction of Human Faces," in *ECCV*, Springer, 2022, pp. 250–269 (cit. on p. 6).

[93] Zielonka, W., Bolkart, T., and Thies, J., "Instant Volumetric Head Avatars," in *CVPR*, 2023, pp. 4574–4584 (cit. on p. 6).

[94] Zins, P., Xu, Y., Boyer, E., Wuhrer, S., and Tung, T., "Data-Driven 3D Reconstruction of Dressed Humans From Sparse Views," 2021 (cit. on p. 18).

[95] Zwicker, M., Pfister, H., Van Baar, J., and Gross, M., "EWA volume splatting," in *Proceedings Visualization, 2001. VIS'01.*, IEEE, 2001, pp. 29–538 (cit. on p. 5).